

# UC San Diego

## UC San Diego Electronic Theses and Dissertations

### Title

Reproducibility of Effects of Vibrational Strong Coupling on Chemical Reaction Rates

### Permalink

<https://escholarship.org/uc/item/9pc1m1wx>

### Author

Wiesehan, Garret Douglas

### Publication Date

2022

Peer reviewed|Thesis/dissertation

UNIVERSITY OF CALIFORNIA SAN DIEGO

Reproducibility of Effects of Vibrational Strong Coupling on Chemical Reaction Rates

A thesis submitted in partial satisfaction of the requirements for the degree Master of Science

in

Chemistry

by

Garret Douglas Wiesehan

Committee in charge:

Professor Wei Xiong, Chair  
Professor Valerie Schmidt  
Professor Joel Yuen-Zhou

2022

Copyright

Garret Wiesehan, 2022

All rights reserved

The thesis of Garret Wiesehan is approved, and it is acceptable in quality and form for publication on microfilm and electronically.

University of California San Diego

2022

## TABLE OF CONTENTS

Thesis Approval Page-----	iii
Table of Contents-----	iv
List of Abbreviations -----	vi
List of Figures -----	vii
List of Tables-----	viii
Acknowledgements -----	ix
Abstract of the Thesis-----	x
Chapter 1: Introduction -----	1
1.1 Reaction Modification by Vibrational Strong Coupling-----	1
1.2 Previously Observed VS Reaction Modifications -----	1
1.3 Ester Hydrolysis of <i>para</i> -Nitrophenyl Acetate-----	3
1.4 Research Objectives and Structure -----	5
Chapter 2: Background -----	5
2.1 Molecular Vibrations -----	5
2.3 Electromagnetic Confinement-----	6
2.4 Vibrational Strong Coupling-----	11
Chapter 3: Methodology-----	13
3.1 Reagent Preparation-----	13
3.2 Reaction Cell Design -----	14
3.4 Fabry-Pérot Cavity Design and Fabrication -----	16
3.5 Fourier Transformed Infrared Spectroscopy Measurements -----	17
3.6 Ultraviolet-Visible Spectroscopy Measurements -----	17
3.7 Reaction Experimental Procedure -----	17
3.8 Reaction Rate Constant Derivation -----	20
3.9 Pathlength Calibration -----	21
Chapter 4: Discussion-----	24

4.1 Out of Cavity Spectra and Rates -----	24
4.2 In Cavity Spectra and Rates -----	25
4.3 Rate Detuning Dependence -----	26
4.4 Polariton Dispersion -----	28
4.5 Three-Oscillator Model-----	30
4.6 Discrepancies of Results -----	38
Chapter 5: Conclusion -----	39
References -----	41

## LIST OF ABBREVIATIONS

ATR	Attenuated Total Reflectance
CaF <sub>2</sub>	Calcium Fluoride
EMF	Electromagnetic Field
EtOAc	Ethyl Acetate
FP Cavity	Fabry-Pérot Cavity
FSR	Free Spectral Range
FTIR	Fourier Transformed Infrared Spectroscopy
FWHM	Full Width Half Max
LP	Lower Polariton
MeOH	Methanol
MP	Middle Polariton
MVP	Molecular Vibrational Polariton
PES	Potential Energy Surface
PNP <sup>-</sup>	<i>para</i> -nitrophenoxide
PNPA	<i>para</i> -nitrophenyl acetate
TBAF	tetrabutylammonium fluoride
UP	Upper Polariton
UV-Vis	Ultraviolet-Visible Spectroscopy
VSC	Vibrational Strong Coupling
$\alpha$ -CT	$\alpha$ -chymotrypsin

## LIST OF FIGURES

Figure 1. PNPA ester hydrolysis reaction equation and mechanism-----	3
Figure 2. FTIR spectrum of reaction solution and reaction solution under VSC -----	4
Figure 3. Diagram of an FP cavity and cavity modes -----	7
Figure 4. FTIR spectrum of an air filled FP cavity -----	9
Figure 5. Image of assembled reaction cell with cavity mirrors-----	15
Figure 6. Diagram of experimental setup -----	19
Figure 7. Pathlength calibration absorption spectra -----	23
Figure 8. Out of cavity reaction UV-Vis spectra and kinetic data -----	24
Figure 9. In cavity reaction UV-Vis spectra and kinetic data-----	25
Figure 10. Detuning dependence of reaction rate constant-----	27
Figure 11. Cavity dispersion curve with 2x2 Hamiltonian and TMM simulations -----	29
Figure 12. FTIR spectra showing solvent effect on EtOAc frequency -----	31
Figure 13. FTIR spectra of pure EtOAc and reaction solvent system -----	32
Figure 14. ATR-FTIR spectra of PNPA and EtOAc -----	33
Figure 14. Three oscillator model results from experimental parameters-----	35
Figure 15. Three oscillator model results from idealized parameters-----	36



## LIST OF TABLES

Table 1. Parameters and Hopfield coefficients of the “realistic” three oscillator model----- 37

Table 2. Parameters and Hopfield coefficients of the “idealized” three oscillator model --- 37

## ACKNOWLEDGMENTS

I would like to thank my advisor and committee chair Professor Wei Xiong, for his support and guidance in my research and growth as a researcher and person. I would like to thank my committee member Professor Joel Yuen-Zhou for his encouragement and mentorship for giving me the opportunity to pursue goals I never thought I'd reach. I would like to thank my committee member Professor Valerie Schmidt, for her crucial advice and guidance as well as reinvigorating my passion for organic chemistry.

I would like to thank the members of the Xiong group, past and present. Always kind and supportive, sharing a deep curiosity for the mysteries of chemistry; this would not have been possible without you. I would like to thank Matthew Du, Jorge Campos-Gonzalez-Angulo, and the Yuen-Zhou group for their mentorship when I was a curious undergraduate. I want to thank Joseph Palaz of the Kubiak group for his assistance and useful discussions. I would like to thank Professor Nathan Romero for his generosity in instrument and lab space use.

I also want to thank Lauren Waller, my girlfriend whose patience, understanding, and loving support continues to motivate me towards ever higher goals. Finally, I want to thank my parents, whose efforts to expose me to science and culture from a young age instilled a curiosity that pushes me ever forward. Their unwavering support for me as I pursue my dreams in science, I will be eternally grateful for.

The material presented is a reprint of the publication by Wiesehan, G. D.; Xiong, W. Negligible Rate Enhancement from Reported Cooperative Vibrational Strong Coupling Catalysis. *J. Chem. Phys.* **2021**, *155* (24), 241103. <https://doi.org/10.1063/5.0077549>. The thesis author was the primary investigator and author of this material.

## ABSTRACT OF THE THESIS

Reproducibility of Effects of Vibrational Strong Coupling on Chemical Reaction Rates

by

Garret Douglas Wiesehan

Master of Science in Chemistry

University of California San Diego, 2022

Professor Wei Xiong, Chair

The ability to conduct new chemical reactions, or to control known reactions in new ways, is a key area of academic and societal interest. In recent years, developments in the field of photonics have revealed phenomena that occur when molecules strongly interact with light. One area of interest is in vibrational strong coupling, which occurs when molecular bond vibrations strongly interact with electromagnetic fields in the mid-infrared regime. In a fascinating series of experiments, reactions were performed under vibrational strong coupling and observed to be

dramatically modified. Given the impact that these findings imply, independent verification and a thorough understanding of the underlying mechanisms is critical. One such reaction, where the ester *para*-nitrophenyl acetate is hydrolyzed by tetrabutylammonium fluoride in ethyl acetate, reportedly accelerated by an order of magnitude. An attempt to reproduce these findings with the goal of further investigating the mechanism of reaction modification is presented. While experimental procedures and conditions were performed closely to those of the original work, no reaction modification was observed. Furthermore, no significant change in reaction rate with detuning was found. An analysis of the reaction system was performed using Jaynes-Cummings coupled oscillator and transfer matrix method models to confirm vibrational strong coupling and investigate the lack of observed reaction modification. The potential of vibrational strong coupling as new tool for reaction control is tantalizing and may usher in a new era of chemical synthesis, however a robust understanding of the underlying mechanisms involved are crucial to its realization.

## **Chapter 1: Introduction**

### **1.1 Reaction Modification by Vibrational Strong Coupling**

The ability to use and control chemical reactions has been a crucial part of human history. The cooking of food, production of soap, and fermentation of wine were crucial components to the development of early societies and cultures. Advances in chemistry through the ages with the discovery of gunpowder, mass producible fertilizers, and the modern pharmaceuticals have each brought massive changes in civilization. It is no surprise that research into new methods to perform and control chemistry remains a frontier of intense interest. In recent years, an intriguing idea has sparked fervent interest with the potential to bring about a new era of chemical synthesis<sup>1</sup>. When placed into a confined optical environment, molecular systems and photons can strongly interact if the energy of a photon in that environment closely matches that of an energy of a transition within the molecule. If a photon mode in this system interacts with a molecular vibrational mode, it is known as vibrational strong coupling (VSC) and the system is known as a molecular vibrational polariton (MVP). Strongly coupled systems demonstrate many intriguing properties, of which a fascinating example is the ability to modulate chemical reactions when participating molecules are strongly coupled.<sup>1-10</sup> However, no clear link between the characteristics of the strong coupling and modification of reaction dynamics or thermodynamics have been made<sup>11-15</sup>.

### **1.2 Previously Observed VSC Reaction Modifications**

Current investigations into the effects that VSC has on molecular processes have been varied<sup>3</sup>. Reactions of a range of complexity have been observed to be modified kinetically, chemo- and stereo-selectively influenced under VSC. In one reported instance, the ester

hydrolysis of PNPA by the enzyme  $\alpha$ -chymotrypsin ( $\alpha$ -CT) was modified when the  $3100\text{ cm}^{-1}$  O-H stretching mode of solvent  $\text{H}_2\text{O}$  and the enzyme was strongly coupled to<sup>16</sup>. The enzyme  $\alpha$ -CT utilizes a serine-histidine-aspartate catalytic triad that acts as a charge-relay system to facilitate ester hydrolysis. It was found that the catalytic efficiency of the hydrolysis increased by seven times when under VSC. In another investigation, the dehydrogenation of ammonia borane was reported accelerated by four orders of magnitude when placed under into an optical cavity tuned to the O-H stretching mode of  $\text{H}_2\text{O}$ <sup>17</sup>. In a reported instance of VSC enabled chemoselectivity, *tert*-butyldimethyl{[4-(trimethylsilyl)but-3-yn-1-yl]oxy}silane, a molecule with two distinct silane groups, was selectively desilated using VSC<sup>18</sup>. When not in a cavity, the reaction followed typical product formation patterns where one silyl group was preferentially cleaved and a ratio of singly desilated products formed. The reaction was then performed in a cavity tuned to Si-C silyl alkyne ( $842\text{ cm}^{-1}$ ), Si-O silyl ether ( $1110\text{ cm}^{-1}$ ), or Si- $\text{CH}_3$  methylsilane ( $1250\text{ cm}^{-1}$ ) vibrational modes. While the uncoupled product ratio favored cleavage of the cleavage of the silyl alkyne bond (60% Si-C scission product, 40% Si-O scission product), the product ratio inverted under VSC with greater selectivity (20% Si-C scission product, 80% Si-O scission product). This finding was thought to be the result of VSC altering the thermodynamic landscape of the reaction, raising the activation barrier of the originally preferred product, and lowering that of the other.

### 1.3 Ester Hydrolysis of *para*-Nitrophenyl Acetate

One curious example of a VSC modified chemical reaction is the cavity catalysis of the hydrolysis of *para*-nitrophenyl acetate (PNPA) by *tetrabutylammonium fluoride* (TBAF) in *ethyl acetate* (EtOAc)<sup>19</sup>. It was found that when placed into a cavity tuned to the vibrational frequencies of the carbonyl stretching modes of PNPA (1759 cm<sup>-1</sup>) and the solvent EtOAc (1750 cm<sup>-1</sup>) the reaction rate constant was accelerated by an order of magnitude. The understood reaction mechanism proceeds by a B<sub>AC2</sub> base-catalyzed acyl hydrolysis. F<sup>-</sup> ions from TBAF perform a nucleophilic attack on the carbonyl carbon of PNPA. A tetrahedral intermediate complex form and subsequently dissociates into acetyl fluoride and *para*-nitrophenoxide (PNP<sup>-</sup>). The reaction rate is determined by the nucleophilic attack step and the ability of F<sup>-</sup> ions to access PNPA carbonyl. Under basic conditions (above pH 7.5), PNP<sup>-</sup> remains in its deprotonated form exhibiting a yellow color resulting from a strong absorption feature at 400 nm. This allows for the in situ kinetic tracking of the reaction by using UV-Visible spectroscopy to observe the growth of this 400 nm feature.

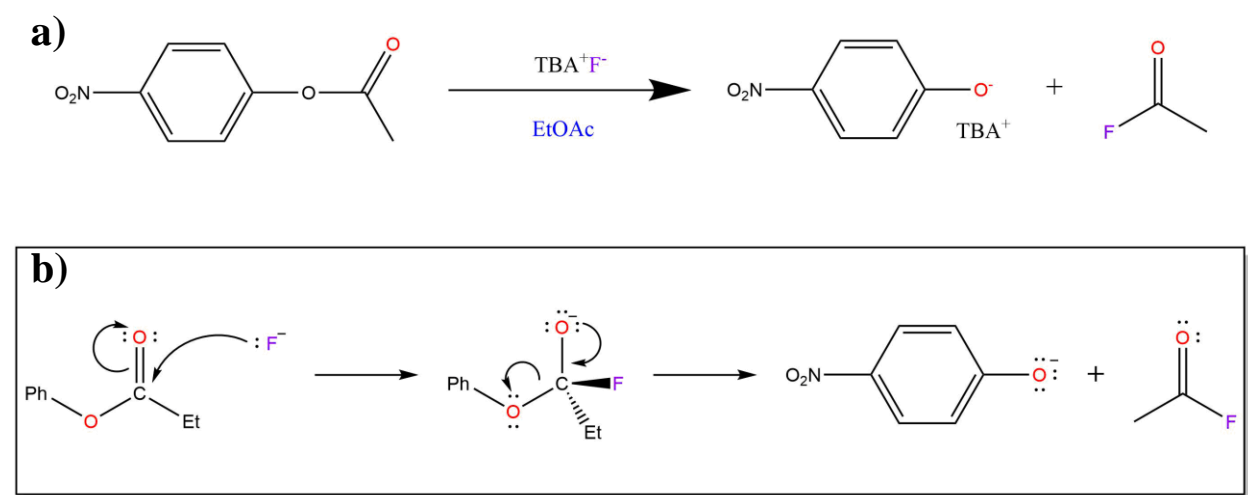


**Fig 1.** (a) Base mediated PNPA ester hydrolysis reaction in Ethyl Acetate (EtOAc). (b) B<sub>AC2</sub> Mechanism of the hydrolysis of PNPA by TBAF. Fluoride anion of TBAF performs a nucleophilic attack on the carbonyl of PNPA. The charged tetrahedral intermediate eliminates *para*-nitrophenoxide leaving acetyl fluoride.

An intriguing aspect of this finding is the nature of the coupling in this system. Concentrations are far too low to achieve VSC by coupling to reactant PNPA alone. Rather than coupling only to a participating molecule in the reaction, the reaction rate acceleration was found to be enabled by *cooperative coupling*. In cooperative strong coupling, the solvent or other non-participating molecule present couples to the same photon mode as the coupled reactant. Since the strength of VSC has a proportional relation to the number of molecules coupled to, the coupling of both reactant and “bystander” molecules cooperatively enhances the strength of overall coupling. With the findings that the degree of reaction modification was linked to the strength of coupling, cooperative coupling may be able to provide a mechanism of control over

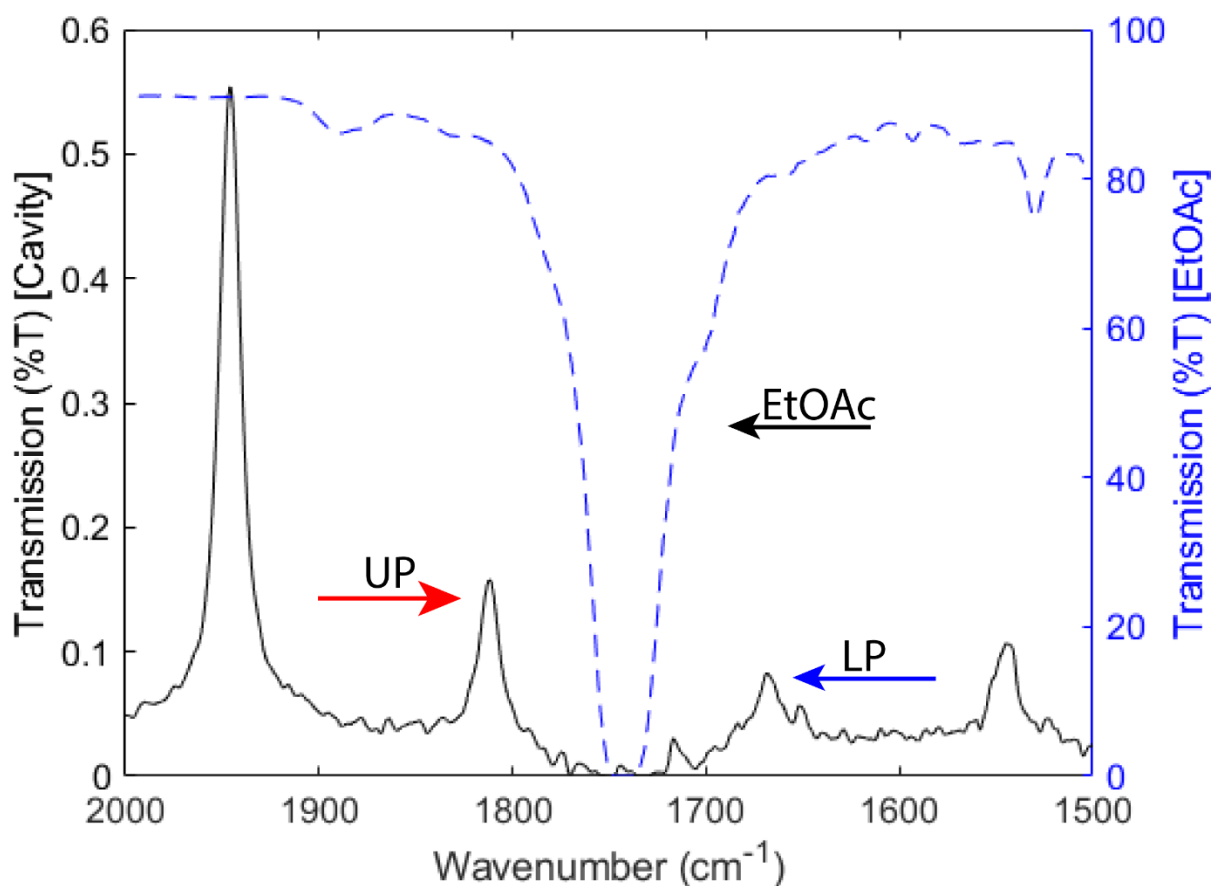


**Fig 2.** FTIR spectra showing EtOAc carbonyl stretching mode absorption centered at  $1740\text{ cm}^{-1}$  (blue dashes) and reaction solution in a FP cavity on resonance with the EtOAc molecular mode. UP and LP values observed here to be  $1811.8\text{ cm}^{-1}$  and  $1668.6\text{ cm}^{-1}$  respectively. The detuning and Rabi splitting was calculated to be  $0.4\text{ cm}^{-1}$  and  $143.2\text{ cm}^{-1}$  respectively.



cavity reactions and give a route of further investigation into the nature of cavity modified reactions.

## 1.4 Research Objectives and Structure

The potential utility of VSC to become a new tool for chemical synthesis is substantial. Effects on some reactions have been dramatic and may open the door to new synthetic routes, ease reactions previously difficult to conduct, or eliminate the need for expensive or harmful reagents and catalysts. To adequately realize this potential and allow the rational design of cavities for the manipulation of reactions, the need for a foundational mechanistic understanding is paramount.

Here presented are the efforts to replicate the observations of Lather et.al.<sup>19</sup> on the cooperative coupling enabled cavity catalysis of the ester hydrolysis of *para*-nitrophenyl acetate.<sup>20</sup> First discussed are the fundamentals of VSC and related concepts followed by a description of the methodology of the attempts to replicate the findings of the ester hydrolysis under cooperative strong coupling by Lather *et.al.* Finally, a discussion and analysis of the findings and further simulations on the system are presented.

## Chapter 2: Background

### 2.1 Molecular Vibrations

Molecules exhibit many complex dynamics which dictate their physical and chemical properties. One category of these dynamics is molecular vibrational dynamics. Molecular vibrations are oscillations in relative atomic positions within a molecular structure. These

molecular vibrations are characterized by their frequency of oscillation which are determined by the masses of two adjacent atoms and strength of the electronic bond between them.

Molecular vibrations are often characterized as quantum harmonic oscillators confined by a potential energy landscape. Molecular vibrations occupy discrete vibrational energy states on a PES. Vibrational modes that occur between atoms where a difference in electronegativity, or dipole, is present, transitions between vibrational states may be induced by infrared radiation that is resonant in energy to the difference in energy of between said states. These vibrational modes are described as *IR active* and are the forms of molecular dynamics of focus in these experiments.

## **2.2 Electromagnetic Confinement**

A key component to formation of VSC systems is the ability to generate environments of precise and strong electromagnetic fields. By far the most common method for strongly coupling with liquid phase reaction studies is the Fabry-Pérot (FP) optical cavity. In basic terms, an FP cavity consists of two partially mirrored surfaces separated by a short distance. When externally pumped, FP cavities allow the transmission of a small number of photons into it. Once inside the cavity, the photon will internally reflect many times, remaining within the cavity for a substantial time. Constructive interference of select frequencies resonant with the cavity generate a high amplitude standing wave of said frequency, resulting in a confined region of space under a potent electromagnetic field. (Fig 3)

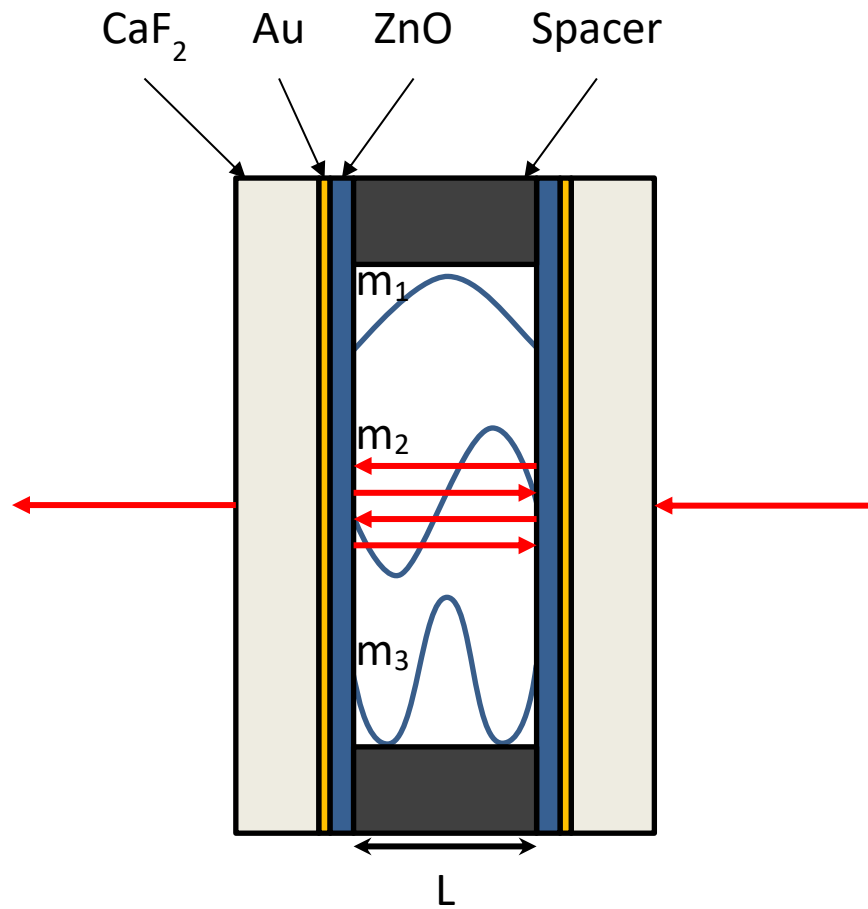


**Fig 3.** Diagram of a Fabry-Perot optical cavity showing incident light and internal reflections within the cavity. Cavity modes showing resonant wavelengths that are  $\frac{1}{2}$  divisible by the cavity pathlength.

An important feature of these optical cavities is their selectivity of frequency and generation of optical modes. When reflecting within the cavity, only EM fields with half wavelengths that are integer proportional to the pathlength of the cavity can exist. The cavity modes in terms of wavenumber can be found using the equation.<sup>2,6,7</sup>

$$\bar{\nu}_m = \frac{10^4}{2nL} m$$

Where  $\bar{\nu}_m$  denotes the wavenumber of the  $m^{\text{th}}$  integer cavity mode and its relationship to the refractive index of the cavity medium,  $n$ , and  $L$ , the pathlength between the cavity mirrors. The EM waves within the cavity must reflect from each surface without shifting phase relative to itself, with each maxima and minima occurring at the same spatial location within the cavity. The result is that these wavelengths are able to constructively interfere with themselves and generate EM fields of high intensity in a confined space. All other wavelengths within the cavity which will continuously shift phase upon each reflection, resulting in their destructive interference.

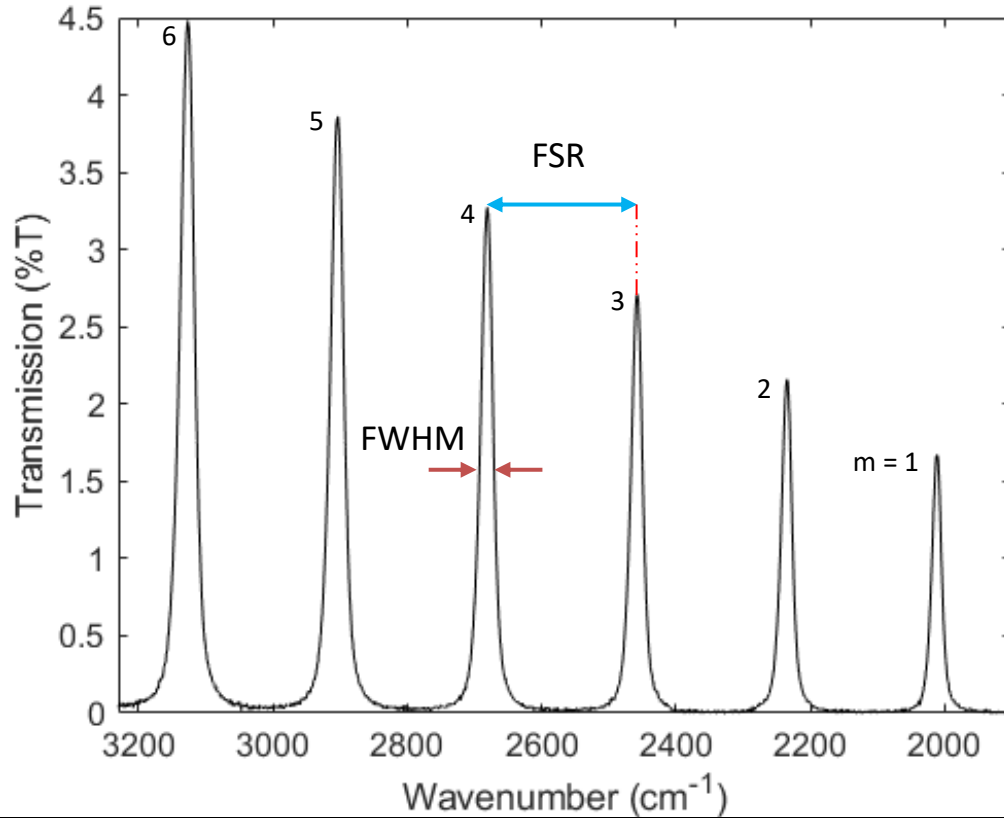


**Fig 4.** Typical FTIR spectrum of an air-filled FP cavity. Resonant cavity frequencies are labeled  $m = 1, 2, \dots, 6$ . FSR (blue arrow) showing the spacing between resonant frequencies and FWHM (orange arrows) of the 4<sup>th</sup> mode.

Other characteristics important to FP cavity performance include the Free Spectral Range (FSR) and quality factor (Q). FSR indicates the distance in frequency each cavity modes lies from one another. (Fig. 4) Within a local frequency domain, it is found simply by the difference in frequency of two adjacent peaks.

$$FSR = \frac{10^4}{2nL} (m_{i+1} - m)$$

It should be noted that FSR also carries the dependence of refractive index and should not be generalized for all frequency domains of the cavity modes. Cavity Q is a dimensionless factor that characterizes the sharpness of each cavity mode. It is a quantification of the cavity's capacity for storing the energy of a given cavity mode. A high Q cavity mode is capable of containing a

photon for a long amount of time and for many reflections, increasing its contribution to the intensity of the mode before dissipating. It can be obtained for a given cavity mode by dividing the mode frequency, by its full width at half its maximum (FWHM).

$$Q = \frac{\bar{\nu}_m}{FWHM}$$

One physical interpretation of cavity Q is the number of round trips that a photon will make inside the cavity. There is no consensus on the importance and influence of Q factor on VSC and associated phenomena. In practice, cavity Q is useful as a tool for the determination of the parallelism when tuning a cavity. Cavity mirrors must be highly parallel to each other to retain a consistent pathlength over an area. Changes in pathlength results in a mixture of resonant modes, broadening the FWHM and lowering the specificity of resonant EM waves.

## 2.3 Vibrational Strong Coupling

The interaction of confined IR light and a molecular vibration can be described as a form of a coupled oscillator. When the interaction of the two becomes great enough, such that the rate of energy exchange between the two oscillators is greater than any other rates of decay, two new energy states emerge. These new states are called the upper polariton (UP) and lower polariton (LP). The strength of the coupling between these oscillators is evident by the difference in energy between these new states given by the equation.<sup>6</sup>

$$h\Omega_R = 2 \sqrt{\frac{\hbar\omega}{2\varepsilon_0 v}} d \sqrt{n_{ph} + 1}$$

The separation in energy of the new states is given by the,  $\Omega_R$ , the rate of energy exchange between the cavity photons  $n_{ph}$  and the molecules contained within the volume of the cavity EMF,  $v$ . Additionally, it is dependent on the resonant energy,  $\hbar\omega$ , vacuum permittivity,  $\varepsilon_0$ , indicating that the coupling is also dependent on the EMF strength. It should be noted that even when  $n_{ph}$  is zero, there is still some exchange of energy with the cavity. This is due to the zero point energy of the cavity, coupling to the vacuum EMF and giving rise to what is known as vacuum Rabi splitting.

A common formalism for describing this strongly coupled systems is with the Jaynes-Cummings model. Here, a single cavity mode,  $\omega_{mol}$ , interacts with molecules which are considered as indistinguishable two level systems with transition energy  $\omega_{mol}$ . These interact with some coupling strength  $g_0$ .

$$\begin{bmatrix} \omega_{cav} & g_0 \\ g_0 & \omega_{mol} \end{bmatrix} \begin{bmatrix} \alpha_{cav} \\ \alpha_{mol} \end{bmatrix} = E \begin{bmatrix} \alpha_{cav} \\ \alpha_{mol} \end{bmatrix} \rightarrow \begin{bmatrix} E_{UP} & 0 \\ 0 & E_{LP} \end{bmatrix} \begin{bmatrix} \alpha_{cav} \\ \alpha_{mol} \end{bmatrix}$$

Upon hybridization, the resulting new eigenstates have energies which represent the UP and LP. Furthermore, the values of  $\alpha_{\text{cav}}$  and  $\alpha_{\text{mol}}$  are called the Hopfield coefficients, which describe the composition of the UP and LP of each the cavity and molecular modes. The energies of the polaritonic modes can be individually described by the equations.

$$E_{UP} = \frac{1}{2} \left[ E_{\text{cav}} + E_{\text{vib}} + \sqrt{4Ng_0 + (E_{\text{cav}} - E_{\text{vib}})^2} \right]$$

$$E_{LP} = \frac{1}{2} \left[ E_{\text{cav}} + E_{\text{vib}} - \sqrt{4Ng_0 + (E_{\text{cav}} - E_{\text{vib}})^2} \right]$$

The difference between  $E_{\text{cav}}$  and  $E_{\text{vib}}$  is known as the detuning, or the degree of mismatch between the energy of the cavity mode and the molecular transition energy.

$$\Delta = E_{\text{cav}} - E_{\text{vib}}$$

When the detuning,  $\Delta$ , is equal to zero, the difference between the  $E_{UP}$  and  $E_{LP}$  yields the Rabi splitting.

$$\Omega = E_{UP} - E_{LP} \propto \sqrt{N}g_0$$

Where  $N$  is the number of coupled molecules and  $g_0$  is the constant which describes the fundamental strength of coupling between cavity and molecule. This is related to the rate of energy exchange by

$$\hbar\Omega_R = \hbar\sqrt{N}\Omega$$

It can be seen from this that the strength of coupling can be strengthened by simply increasing  $N$ .<sup>6</sup> The criteria for strong coupling is such that  $\Omega$  is greater than the average FWHM of the cavity and molecular modes, both indicators of decay rates



The effects of the formation of these new hybrid light-matter modes on molecules undergoing reactions is a hotly debated mechanism.<sup>11,21–23</sup> Shifts in the energy of these modes is thought to alter potential energy surfaces which reactions are dictated by.<sup>24</sup> Furthermore, it is of note that the coupling strength is dependent on the number of molecules within the cavity. In cooperative coupling, as discussed in this work, the

## **Chapter 3: Methodology**

### **3.1 Reagent Preparation**

Caution was taken to ensure purity of reagents to exclude any other substances in the reactants and solvents. PNPA will degrade over time to produce the reaction product PNP<sup>-</sup>, additionally, PNPA and ethyl acetate can degrade to produce acetic acid. Since the growth of the reaction product PNP<sup>-</sup> is being used to follow the reaction progress, it is necessary to remove any present in the starting material. Furthermore, PNP<sup>-</sup> will only exhibit its characteristic 405 nm absorbance feature at when deprotonated at pH above 7.5. The presence of acetic acid from PNPA or ethyl acetate will potentially partially or fully protonate the reaction PNP<sup>-</sup> and artificially lower the absorbance of the product as its produced.

To ensure reagent purity, new bottles of methanol and ethyl acetate were purchased from the university stockroom. Additionally, new 5 g PNPA and 10 g of TBAF trihydrate bottles were purchased from Sigma-Aldrich. A small column of basic alumina was prepared and approximately 400 mL of EtOAc was flashed through to remove any trace acetic acid. To remove any water content from the solvents, the EtOAc and roughly 200 mL of MeOH was then passed over columns of silica gel (60 Å, 230-400 mesh). The initial 25 mL of each eluent was discarded, and the remaining solvents were collected into jars containing anhydrous sodium

sulfate. The prepared solvent jars, along with the PNPA and TBAF bottles were stored in a vacuum desiccation jar when not required for experiments.

### **3.2 Reaction Cell Design**

All spectra were taken and conducted in a transmission FTIR liquid flow cell purchased from Specac Ltd. UK (Figure 5). The cell consists of a stainless-steel housing and a steel cover plate with four mounting screws and two Swagelok fitted channels. Two  $\text{CaF}_2$  windows held between the housing and cover plate with the transmission pathlength set by a mylar spacer inserted between the windows. To set the cell pathlength to the desired 18  $\mu\text{m}$ , a 12  $\mu\text{m}$  and a 6  $\mu\text{m}$  mylar spacer were stacked and inserted. To allow liquid samples to be flowed into and out of the cell, dilled holds in the top  $\text{CaF}_2$  window align with the channels in the cover plate and provide a clear path in and out of the cell's internal volume. A large slot in both plates allows transmission of light through the cell windows and internal volume for spectroscopic observation of a sample.

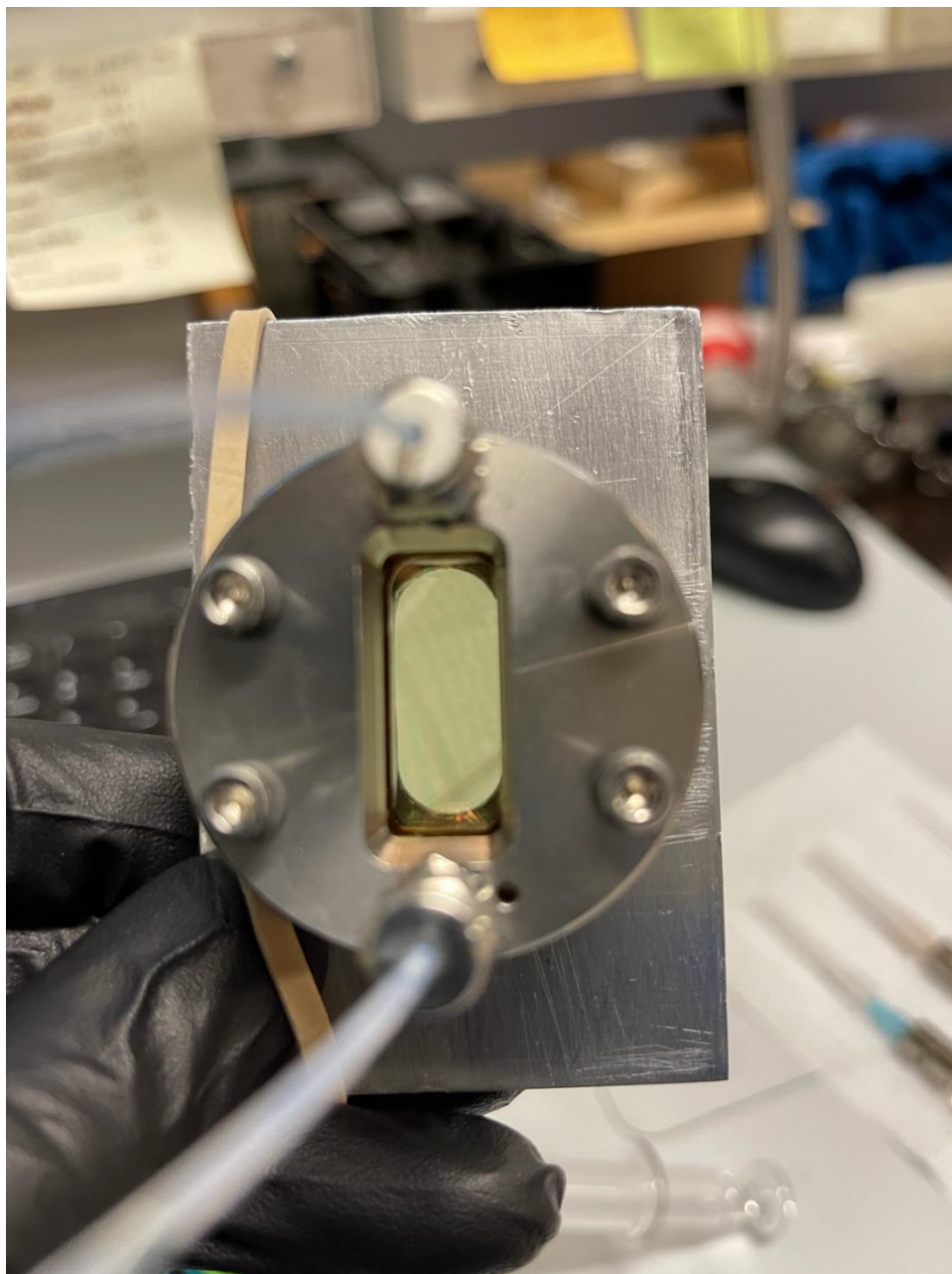


**Fig 5.** Image of the reaction cell assembled with cavity mirrors and tubing attached. The four bolts, two left and two right of the central channel are tightened or loosened to set the pathlength, detuning, and parallelism of the cavity. Note the diagonal lines stemming from the thin film interference pattern between the mirrors.

### 3.4 Fabry-Pérot Cavity Design and Fabrication

In reactions observed under strong coupling, the reaction system was conducted in an optical cavity capable of generating the strong optical modes with which the reactant molecules were able to couple. The overarching design of the optical cavity was that of a Fabry-Pérot cavity, where two partially reflective surfaces are fixed at a set distance from one another. The reaction cell was able to be converted to a Fabry-Pérot cavity through modification of the  $\text{CaF}_2$  windows. Sputter deposition was used to convert the windows into cavity mirrors using a Denton 18 and a Denton 635 sputter coater. The windows were first coated with approximately 2 nm of chromium to provide improved surface adhesion. This was followed by 10 nm of gold to produce a mirrored surface. Roughly 100 nm of ZnO was deposited to insulate the metallic surfaces from damage and prevent them from influencing any chemical reaction they are exposed to. The fabrication yielded surfaces with a reflectivity of ~95% to 5  $\mu\text{m}$  Mid-IR light and 36% to 400 nm visible light.

Once the mirrors were fabricated and inserted into the reaction cell, FTIR spectra confirmed the presence of cavity modes roughly matching the expected features from an 18  $\mu\text{m}$  cavity. To precisely control the cavity detuning and Q-factor, fine control of the mirror parallelism and spacing was performed using the mounting screws in the cell cover plate. By slightly adjusting tension on each screw, the pressure applied to the top mirror and spacer was able to be manipulated. Continuous FTIR spectra was taken as each screw was adjusted until the desired detuning for a given experiment was obtained.

### 3.5 Fourier Transform Infrared Spectroscopy Measurements

FTIR is a crucial component of any VSC experiment. Providing rapid quantitative data for the identification of chemical compounds and their vibrational features as well as the characteristics of strongly coupled systems. All IR spectra taken during this investigation were performed using a ThermoFischer Nicolet iS50 FTIR. Preliminary steps into the replication of the work by Lather et.al. was FTIR analysis of the reagents and solvents of study. Additionally, the FTIR technique of Attenuated Total Reflectance (ATR) was employed to study the C=O stretching mode frequencies of EtOAc and PNPA. In cavity reactions required FTIR spectra taken prior to performing reaction kinetics to record the nature of the coupled system. LP and UP of the EtOAc-PNPA VSC system were recorded to determine detuning as to correlate the relationship to any changes in reaction rate. Cavity Q and Rabi splitting were also extracted before for each reaction.

### 3.6 Ultraviolet-Visible Spectroscopy

Kinetic data was collected using an Agilent Cary 60 UV-Visible spectrometer. Growth of the PNP<sup>-</sup> peak at 400 nm was recorded using scanning kinetic spectra collecting a full spectrum every ~1.2 seconds. The cell and associated experimental hardware were mounted into the instrument using simple hardware. The setup and mounting allowed for closure of ambient light shielding, encasing the entirety of the setup within the instrument during collection.

### 3.7 Experimental Procedure

The overarching design of the cell reaction setup consists of four gas syringes connected to a septum sealed conical vial which in turn leads to the reaction cell. (Figure 6). Two syringes contain the desired quantities of each reactant solution. A third syringe contains air and acts as a

driving piston, to apply headspace pressure and pneumatically drive fluids through the tubing and cell. Lastly, the fourth syringe contains a large quantity of EtOAc to flush out prior reactant residues for subsequent reactions. The conical vial acts as a staging chamber allowing for the rapid combination and mixing of reagents before injection into the cell. Tubing from the conical vial connects to one port of the reaction cell. The second port of the cell is then connected to a waste vial, also septum sealed with an additional venting port. This design allows for the rapid reaction initiation, injection, spectroscopic analysis, and purging all while the cell is mounted within a spectrometer. Several reactions can be performed in series without moving the cell, minimizing any disturbances to minute characteristics of the cell or cavity.

Prior to initiating any reaction series, two stock solutions of reagents were prepared. Stock solutions of PNPA in EtOAc (0.1 M) and TBAF in MeOH (0.1 M) were prepared and set aside. Initial series of reaction experiments were conducted out of cavity to verify the ability to use the cell and associated setup. These reactions were also used to establish the out of cavity baseline reaction rate constant to compare with cavity coupled rates. The cell was mounted into the UV-Vis spectrometer and a background was taken using a 9:1 mixture of EtOAc and MeOH. 90  $\mu\text{L}$  of the PNPA solution and 10  $\mu\text{L}$  of the TBAF solution were loaded into the reactant syringes to achieve the desired 9:1 ratio. Both reactants were injected into the conical vial, quickly shaken to mix, and injected into the cell. Full spectra from 375 nm to 425 nm were taken at 1.5 second intervals from 0 to 600 seconds to follow the growth of the 400 nm  $\text{PNP}^-$  absorption band. From 600 to 3600 seconds, spectra were taken every 60 seconds to observe the final absorbance at reaction completion.

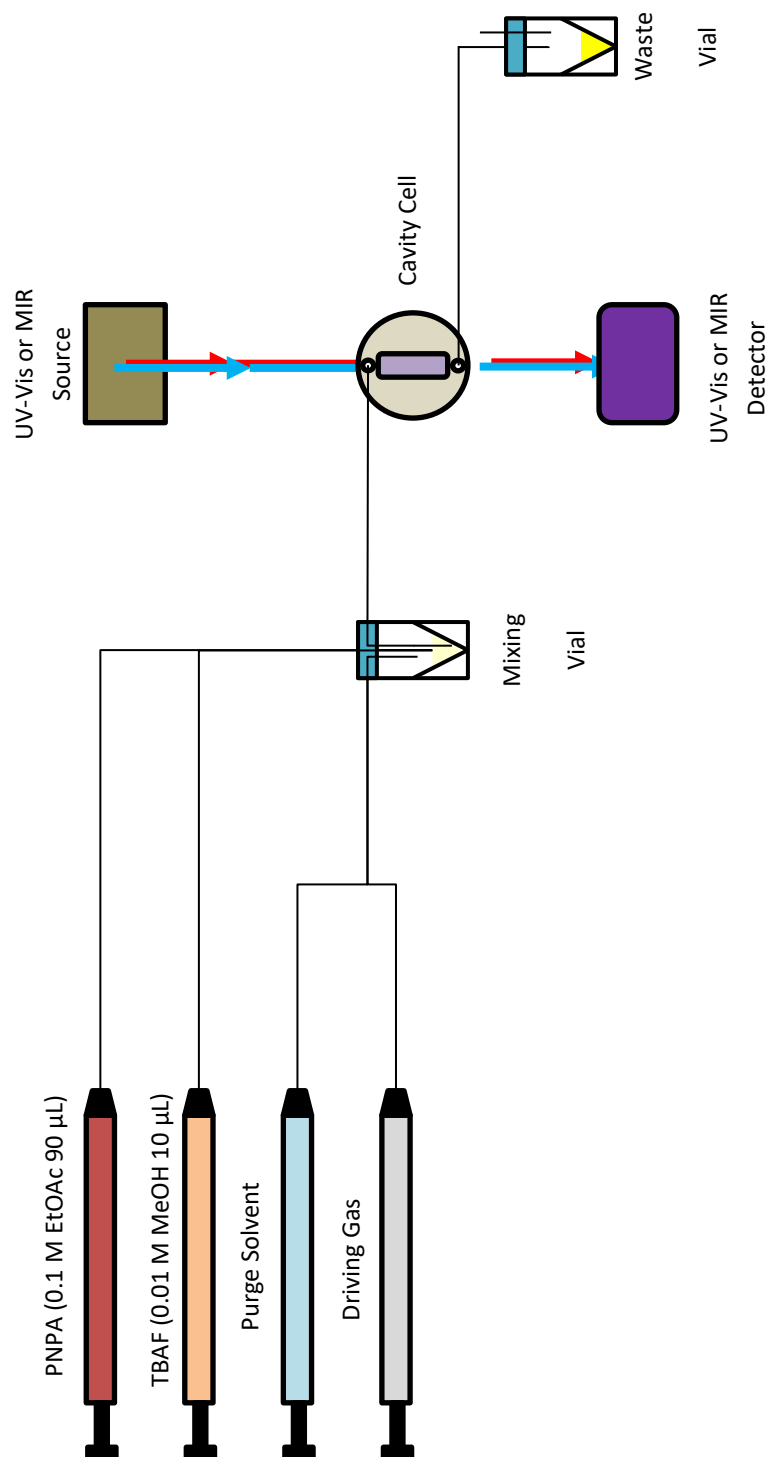


**Figure 6.** Scheme of reaction setup showing four syringes containing reaction solutions, solvent, and gas connected to the mixing vial and then to the transmission cell. The cell is mounted into an FTIR or UV-Vis spectrometer, allowing for collection of either type of data and the rapid injection or resetting of cell samples while still mounted.

Once the ability to use this procedure and design to observe the reaction kinetics, in cavity reactions were then conducted. The procedure for observing VSC reactions was similar to that of the uncoupled reactions but required additional tuning of the cavity by FTIR. To do this, the cell's windows were replaced with cavity mirrors and mounted into the FTIR. The PNPA component (PNPA 0.1M in EtOAc) of the reaction mixture was injected into the cavity and FTIR spectrum was taken. Slight adjustments to the cell's mounting bolts were made to apply small changes to the pressure of the cavity spacer. Repeated FTIR was taken after each change to observe the change in the UP, LP and Q factor. Once the desired cavity characteristics were reached, the cavity was allowed to rest for 30 minutes. This was done to allow for small shifts in cavity pathlength resulting from the swelling of the mylar spacer as it is exposed to reaction solvent. Additionally, any leaks from the cell would be detected at this time. If a large drift from initial conditions was found after 30 minutes, corrections would be made by small changes to the cell's screws until the cavity mode drifting ceased. Following this, the cavity was transferred to the UV-Vis and the kinetic observation procedure was conducted in identical manner to the out of cavity reactions.

### 3.7 Reaction Rate Constant Derivation

Derivation of the reaction rate constant for the reaction was extracted from the kinetic UV-Vis absorption growth using first order kinetics.<sup>25</sup> The time dependence of the 400 nm peak was obtained by averaging the absorbances between 395-405 nm for each time step.

$$A(t) = \frac{\sum_{i=395}^{405} A_i(t)}{10}$$



The strongest modification in reaction rate would be most evident at early reaction time. This trace was obtained for  $t = 0-300$  seconds. Since the rate constant is derived from growth of product rather than from depletion of reactant, a final absorbance once the reaction is complete is required to calculate the relative rate of reaction. Absorbance at  $t = 3600$  was used for this final  $A_{\text{inf}}$  value unless the cell dried out or any other disturbance occurred. In cases where the trace was disrupted before  $t = 3600$ , the final valid absorbance was taken unless the disruption occurs before 2000 seconds. First order reaction rate treatment was then applied to yield the reaction kinetic trace.

$$kt = -\ln\left(1 - \frac{A(t)}{A_{\infty}}\right)$$

Linear fitting was applied to this series, the slope of this fitting was held as the observed reaction rate.

### **3.8 Pathlength Calibration**

Analysis of the growth of the reaction products relies on the measurement of linear absorbance of 400 nm light. Following the Beer-Lambert Law, the concentration of the reaction product is correlated to the absorbance, pathlength, and extinction coefficient. In order to accurately characterize the growth of reaction product both in cavity and non-cavity, it was crucial to confirm the effective pathlength was the same. Due to the performance of the cavity relying on constructively interfering reflections within, it was necessary to consider that the 400 nm light may make multiple passes through the cavity before exiting. This would artificially increase the absorbance of the in-cavity reaction products by increasing the effective pathlength.

The calibration of the effective pathlengths between the cavity and non-cavity cells, a set of solutions of ferrocene was prepared by serial dilution. A 750 mM stock solution of ferrocene in toluene was first prepared and 5 dilutions were performed down to 125 mM. Ferrocene was selected due to its reasonably high absorption coefficient and its absorption peak of 440 nm being near that of the 400 nm of the reaction product. UV-Visible spectra were taken of the ferrocene solution series both in cavity and out of cavity in cells (Figure 7a-b) with 18  $\mu\text{m}$  spacers and similarly tensioned bolts. The resulting calibration curves were treated with a linear fitting, solving for pathlength (Figure 7c). The result demonstrated a negligible difference in effective pathlengths of 19.67  $\mu\text{m}$  and 19.54  $\mu\text{m}$  for the bare cell and cavity respectively.

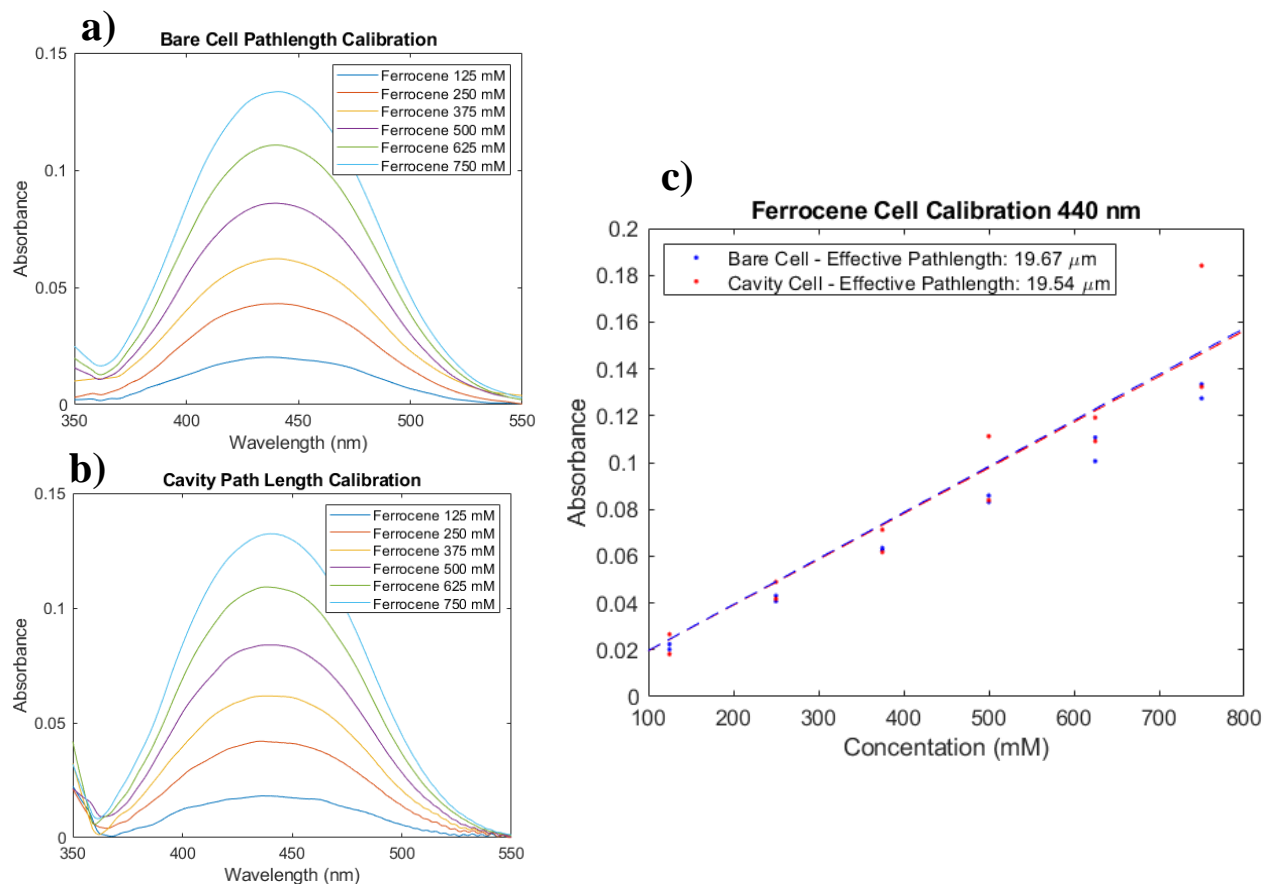


**Fig 7.** (a) UV-Vis spectra of ferrocene calibration solutions in bare cell with uncoated  $\text{CaF}_2$  windows. (b) UV-Vis spectra of ferrocene calibration solutions in cavity cell with mirrored  $\text{CaF}_2$  mirrors. (c) Data from two independently created ferrocene calibration solutions observed in the bare cell (blue) and cavity cell (red). Linear absorbance fitting shown by dashed lines.

## Chapter 4: Discussion

### 4.1 Out of Cavity Spectra and Rate Constant

The first reactions performed were done in a non-cavity cell. A series of five reactions were performed where the growth of the 400 nm absorption feature was observed (Figure 8a). Absorbance values at wavelengths between 395 and 405 nm were averaged and plotted against time (Figure 8b). Once the data was treated with the previously discussed kinetic treatment, as (Figure 8c) an out of cavity reaction rate constant of  $1.5 \times 10^{-3} \pm 2.9 \times 10^{-4} \text{ s}^{-1}$ . This rate was reasonable and in agreement with the previously observed literature value of  $2.0 \times 10^{-3} \text{ s}^{-1}$ .

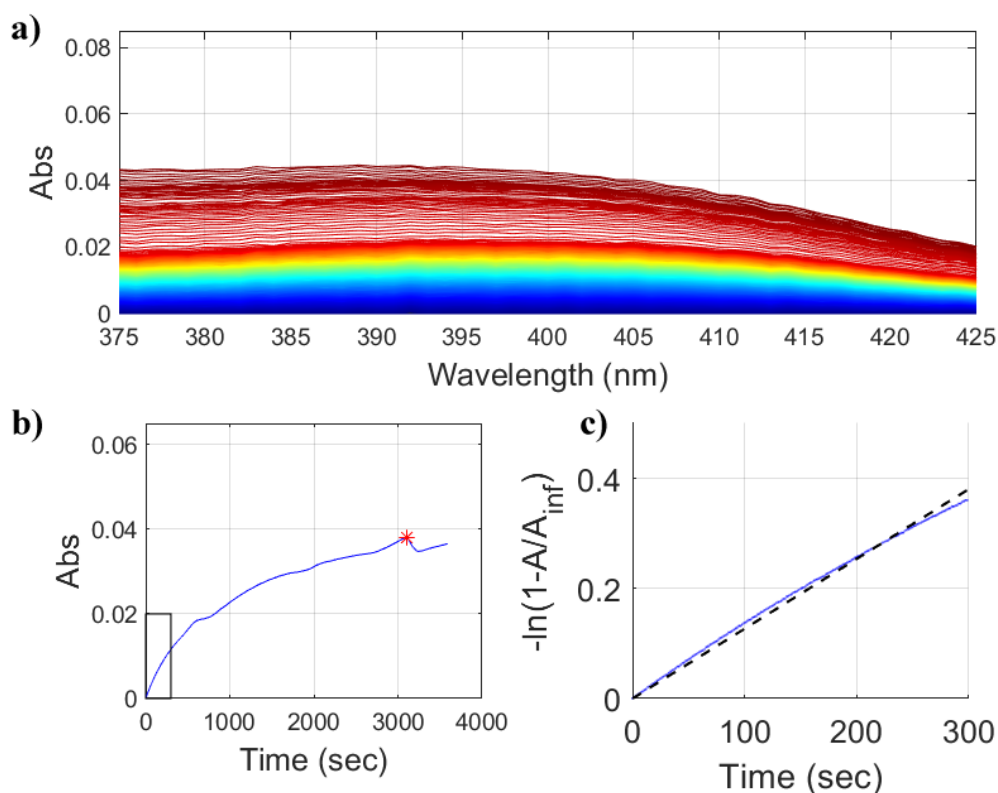


**Fig 8.** (a) Scanning kinetic spectra of out of cavity reactions from 375 to 425 nm showing the growth of the PNP<sup>+</sup> peak. Time resolution of spectra is approximately 1.2 seconds from  $t=0$  to 600 seconds; spectra are taken every 60 seconds from  $t=600$  to 3600 seconds in order to obtain completed reaction absorbance. (b) Kinetic trace of spectra obtained by averaging spectra across all scanned wavelengths at each time step. Red star denotes absorbance value where  $A_{\text{inf}}$  is taken.  $A_{\text{inf}}$  is taken before  $t=3600$  seconds if dramatic changes in absorbance averages occur. (c) Early timescale reaction trace (highlighted in the black box in b) zoomed in to  $t=0$  to 300 seconds, first order kinetics using  $A_{\text{inf}}$  (blue plot) and accompanying linear fitting (black dashes).

## 4.2 In Cavity Spectra and Rate Constant

Prior to all in cavity reactions, FTIR measurements (Figure 2) were taken and display the variety of cavity conditions investigated for cavity catalysis. While the VSC system's Rabi splitting remained roughly static at  $\sim 145\text{ cm}^{-1}$ , FTIR showed a range of cavity FSR between  $154\text{ cm}^{-1}$  and  $182\text{ cm}^{-1}$ . However, the majority of FSR observations were near the  $175\text{ cm}^{-1}$  reported by Lather et.al. Furthermore, the FWHM of cavity modes were  $\sim 16\text{ cm}^{-1}$  (vs  $\sim 20\text{ cm}^{-1}$  in Ref<sup>19</sup>) with a resulting Q-factor of 125 (vs  $\sim 96$  in Ref<sup>19</sup>) when filled with methanol. Reactions were conducted at a range of detunings where  $\Delta = \mp \sim 80\text{ cm}^{-1}$  with a higher density of reactions conducted near  $0\text{ cm}^{-1}$  detuning.

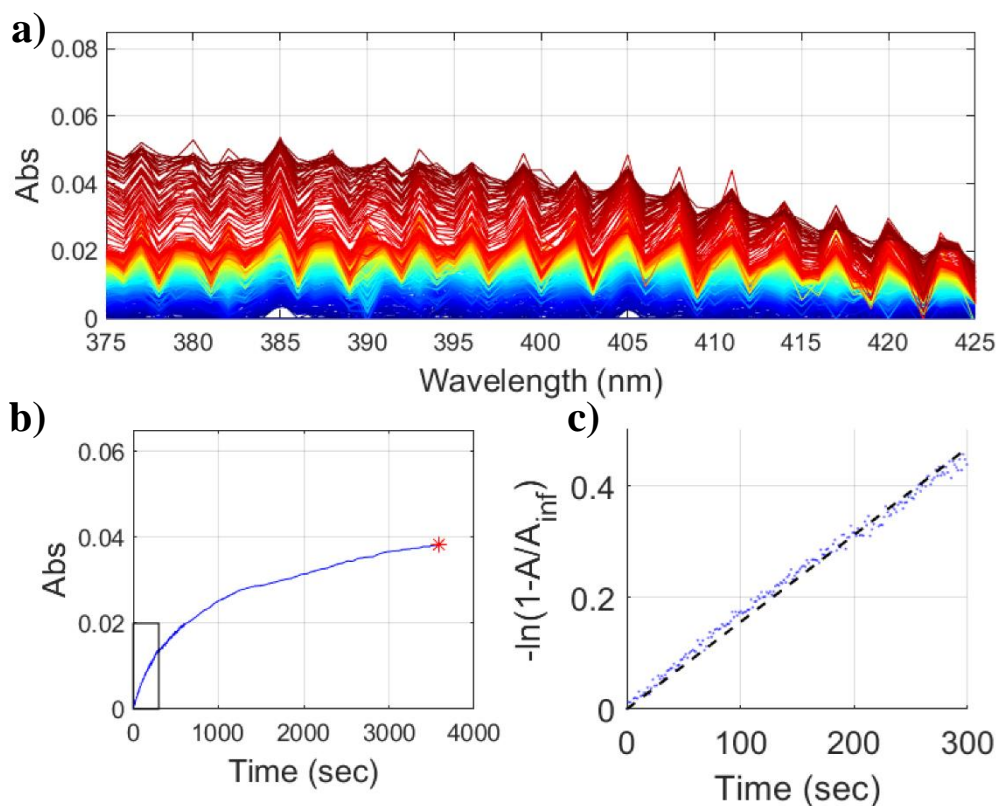


**Fig 9.** (a-c) Same plots as figure 2a-c under VSC. Fringe pattern is evident and appears to be linked to the cavity mode Q factor.

In total, 28 in cavity reactions were performed and display the diversity of cavity characteristics, with an example shown in Figure 9. Fringe patterns were observed in the UV-Vis spectra stemming from the moderately high Q the cavity had in the 400 nm regime and seemed to correlate to Q observed at in FTIR spectra. At zero detuning ( $\omega_{\text{cav}} = \omega_{\text{vib}} = 1740 \text{ cm}^{-1}$ ), the rate constant was found to be  $1.5 \times 10^{-3} \mp 1.0 \times 10^{-4} \text{ s}^{-1}$ . Overall, the reaction rate constant varied between a minimum of  $1.3 \times 10^{-3} \text{ s}^{-1}$  and a maximum of  $2.5 \times 10^{-3} \text{ s}^{-1}$ . Due to the reported C=O mode frequency being  $1750 \text{ cm}^{-1}$  in Ref<sup>19</sup>, the cavity was also tuned to this frequency, where the rate constant was observed to be  $1.75 \times 10^{-3} \text{ s}^{-1}$ . Thus, there was not found to be any significant change in reaction rate constant when under VSC.

#### 4.3 Rate Detuning Dependence

A striking feature in Lather *et.al.*<sup>19</sup> was the high influence that the cavity detuning with the C=O mode of EtOAc and PNPA had on the rate constant modification. The reaction modification was constrained to a narrow detuning interval around  $1750 \text{ cm}^{-1}$ . Reactions were conducted across a wide range of detuning in order to thoroughly investigate this detuning dependence. (Figure 10) There was no clear trend in collected data between detuning and reaction rate constant. Furthermore, the data was binned into detuning regimes, averaging rates over several ranges of detuning. The data, shown in Figure 10, demonstrated few outliers and a narrow range, with the rate distribution and average mostly aligning with that of the uncoupled system. The largest outlier was a 60% enhancement at  $+50 \text{ cm}^{-1}$  of detuning. However, this observation is uncertain due to the sparsity of data at that detuning region. The relative standard deviation was approximately 20%, likely due to the difficulty in precision when working with such small volumes ( $10 \text{ }\mu\text{L} + 90 \text{ }\mu\text{L}$ ).

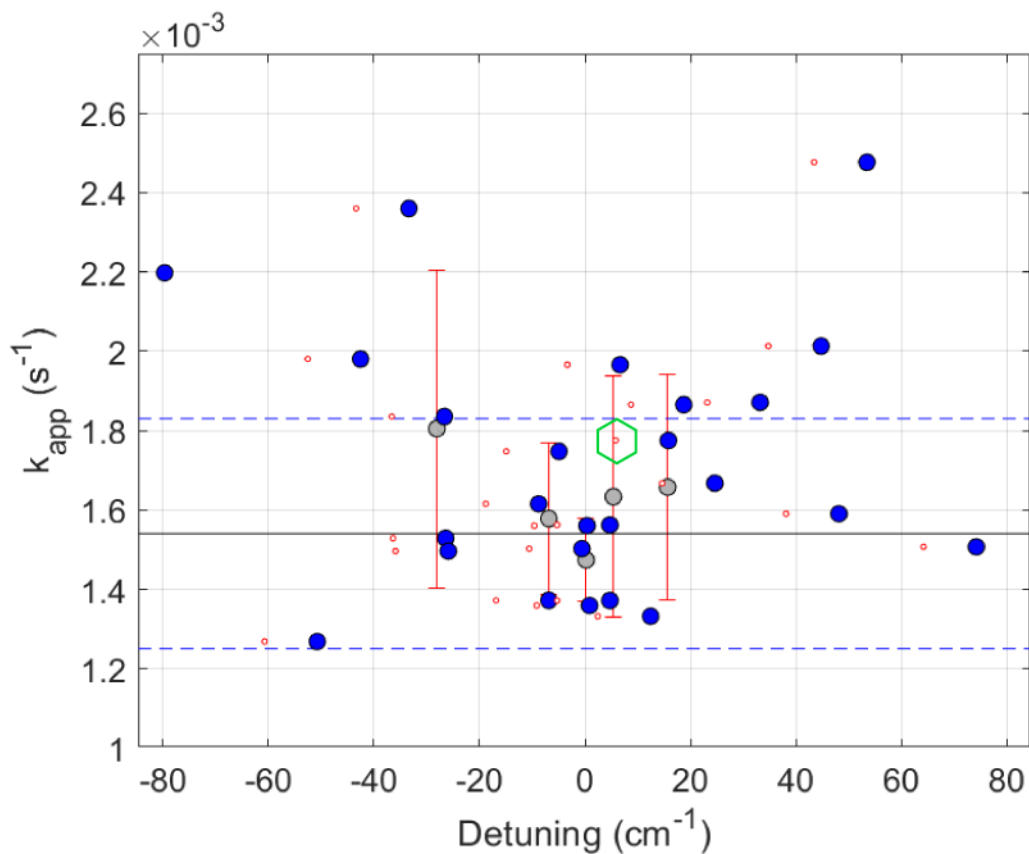


**Fig 10 .** Reaction summary showing reaction rate vs detuning. Individual in-cavity reactions denoted by blue dots. Grey dots represent groupings of detuning regimes and associated distribution of rate constants. Out of cavity reaction average and error shown by black solid and blue dashed lines. Red dots display the same data set with detuning adjusted for  $\omega_{mol} = 1750 cm^{-1}$ .

Despite these facts, should the order of magnitude enhancement and strong cavity detuning dependence exist in the VSC system, it should be distinct in the data.

#### **4.4 Polariton Dispersion**

Due to the Rabi splitting ( $\sim 145\text{ cm}^{-1}$ ) being near that of the FSR of the cavity ( $\sim 175\text{ cm}^{-1}$ ), it was difficult to discern neighboring, uncoupled cavity modes from the LP and UP. This difficulty complicated the accurate assessment of the detuning of the system. To verify calculated detunings and support the assessment that the system truly is under VSC, a dispersion curve was constructed using the FTIR data collected before each reaction. (Figure 11a). Here, the cavity energy is varied by adjusting the pathlength of the cavity by changes to the tension of the cell's bolts while all spectra are taken at normal incidence.



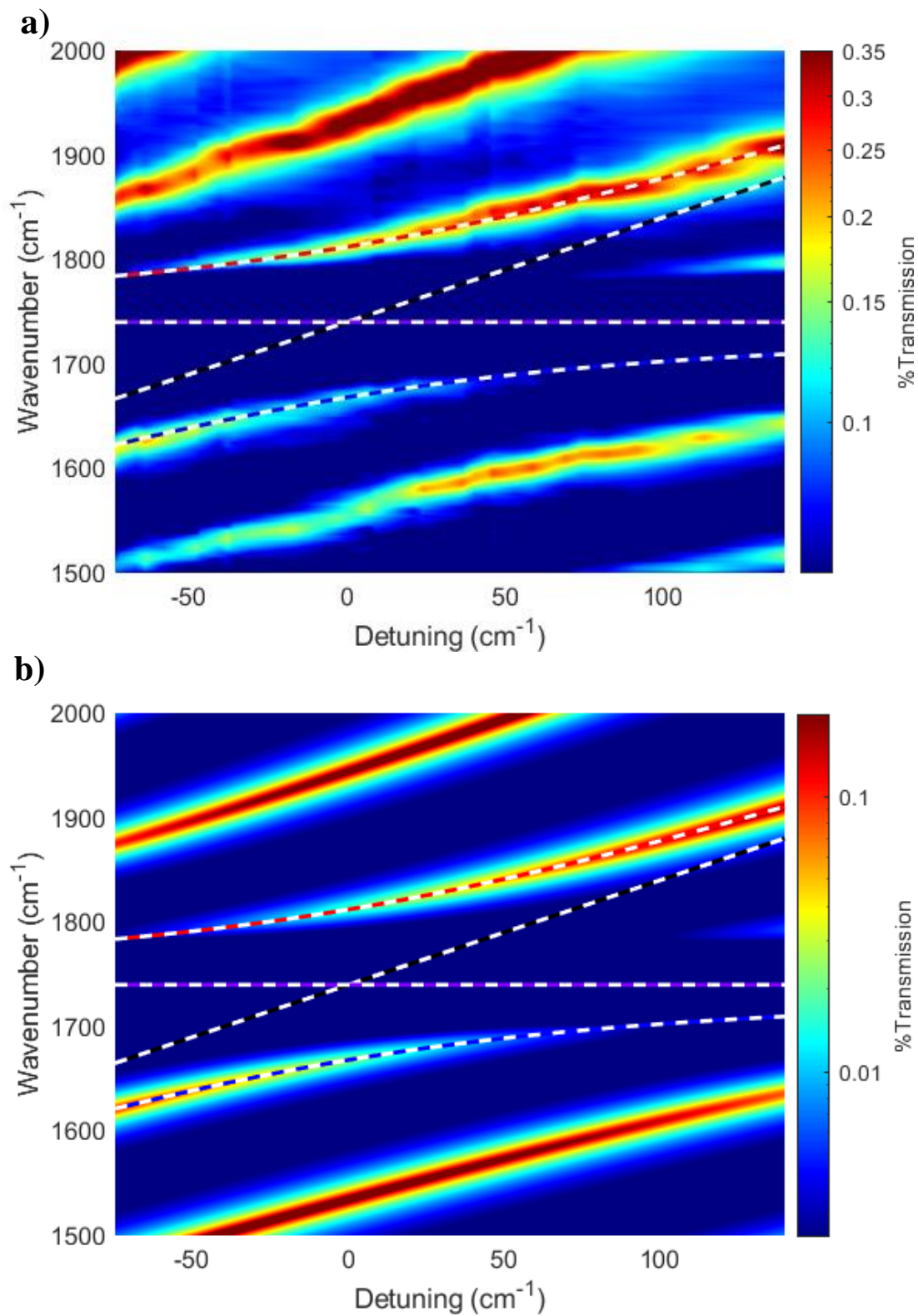


**Fig 11.** (a) Dispersion of polaritons made by EtOAc filled cavity. Spectrum is obtained by taking FTIR of the cavity at roughly equally distributed detunings set.. UP and LP frequencies simulated from the 2-by-2 Hamiltonina are denoted by red and blue dashed lines. Photon and molecular modes are shown by purple and black dashed lines. (b) TMM simulation of  $\text{CaF}_2$  cavity with 96% reflectivity and medium parameters representing EtOAc.

A 2x2 Hamiltonian was constructed to simulate the strongly coupled system in order to compare peak polariton peak positions in the dispersion curve to. The 2x2 Hamiltonian was first constructed with a vibrational mode and a cavity mode fixed at  $1740\text{ cm}^{-1}$ , representing a zero detuning system. Coupling constant was varied until the resulting Rabi splitting upon diagonalization was matched with that of the experimental data ( $145\text{ cm}^{-1}$ ). The coupling constant was found to be  $g = 72$ . The cavity mode was then varied, producing a numerically produced dispersion curve. When overlayed onto the dispersion curve, shown in Figure 11a from FTIR data, the UP and LP energies from the model track well with the experimental data. UP and LP energies display an avoided crossing feature and the greatest Rabi splitting occurs at the zero detuning conditions in both simulated and experimental data.

To further confirm the results of the dispersion curve, a transfer matrix model was constructed to simulate the transmission spectra of the cavity (Figure 11b). The parameters for a  $\text{CaF}_2$  cavity with 96% reflectivity and refractive medium matching that of EtOAc were used in the simulation. This simulation was then compared with the 2x2 Hamiltonian model in a similar manner to the experimental data.

These simulations assist in confirming that the system is indeed showing strong coupling to the EtOAc molecular mode and that the detuning calculated for the spectra are accurate.

#### **4.5 Three Oscillator Model**

A notable difference in the work presented here and the literature is the carbonyl absorption frequencies of EtOAc. In Lather *et.al.*<sup>19</sup> the vibrational frequency of EtOAc was observed to be  $1750\text{ cm}^{-1}$  when measured in 10% (v/v) hexanes. In the work currently presented, the vibrational frequency of EtOAc was found to be  $1742\text{ cm}^{-1}$  when measured in the reaction

EtOAc:MeOH 9:1 conditions by transmission FTIR. The vibrational frequency of PNPA carbonyl was found to agree with Lather *et.al.*<sup>19</sup> at 1758 $\text{cm}^{-1}$ . Relative vibrational energy is a key factor in the cooperative coupling phenomenon, as the vibrational modes must be close in energy to cooperatively strongly couple with the same cavity mode. Further exploration of the vibrational frequency of EtOAc was found to show a significant variance in the position. Transmission spectra of EtOAc in chloroform (0.5 M), and hexanes (0.1 M) yielded vibrational frequencies of 1733  $\text{cm}^{-1}$  and 1749  $\text{cm}^{-1}$  respectively (Figure 12). Spectra of pure EtOAc and reaction conditions of EtOAc:MeOH 90% (v/v) taken at  $>1\text{ }\mu\text{m}$  show vibrational frequencies of 1742  $\text{cm}^{-1}$  (Figure 13). Finally, ATR-FTIR was collected of EtOAc and PNPA films and produce

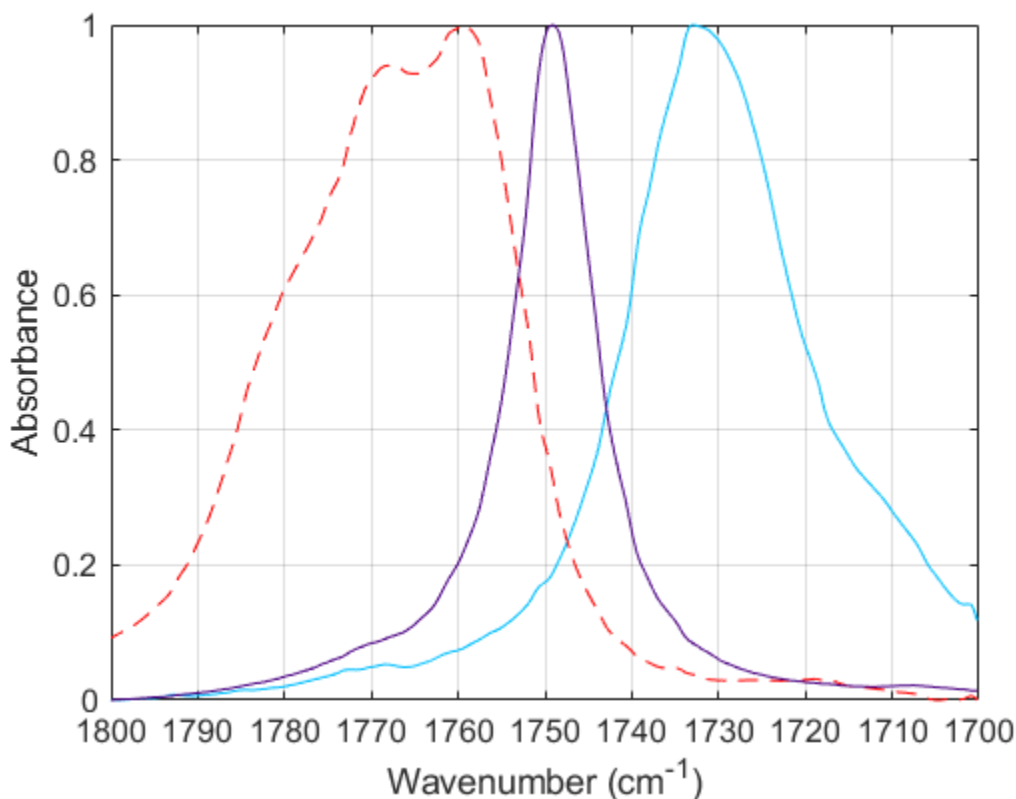


**Fig 12.** Transmission FTIR spectra of ethyl acetate 0.5 M in  $\text{CHCl}_3$  (cyan) and hexanes 10% v/v (purple) with peak absorbance at 1733  $\text{cm}^{-1}$  and 1749  $\text{cm}^{-1}$  respectively. PNPA 0.5 M in  $\text{CHCl}_3$  (red dash) with peak absorbance at 1758  $\text{cm}^{-1}$ . All spectra taken in standard IR transmission cell, 12  $\mu\text{m}$  pathlength with  $\text{CaF}_2$  windows. All spectra shown are normalized to an absorbance value of 1.

vibrational modes of  $1740\text{ cm}^{-1}$  and  $1758\text{ cm}^{-1}$  respectively (Figure 14). Indeed, the solvent effects have a substantial impact on the carbonyl mode of EtOAc, with a variance of vibrational frequency of up to  $38\text{ cm}^{-1}$ .<sup>26</sup> These findings provide insight into a key factor in cooperative coupling and VSC catalysis in general.

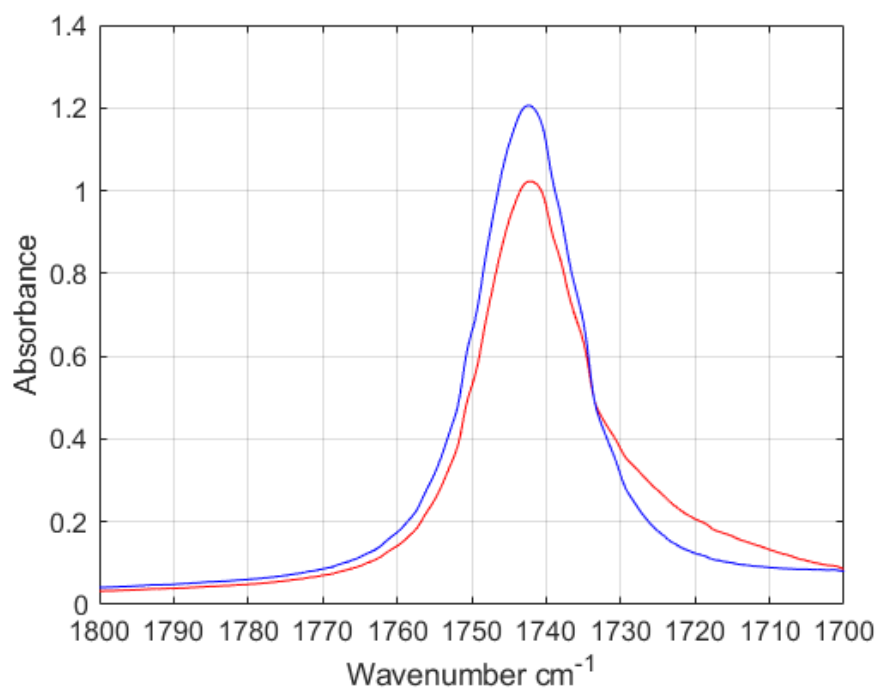


**Fig 13.** Transmission FTIR of pure EtOAc (blue) and an EtOAc-MeOH solution (9:1 ratio) (red). Note asymmetry and shoulder of EtOAc-MeOH at  $1735\text{-}1700\text{ cm}^{-1}$ . Both vibrational modes show peaks at  $1742\text{ cm}^{-1}$ . Spectra taken at extremely short pathlength ( $>1\text{ }\mu\text{m}$ ).

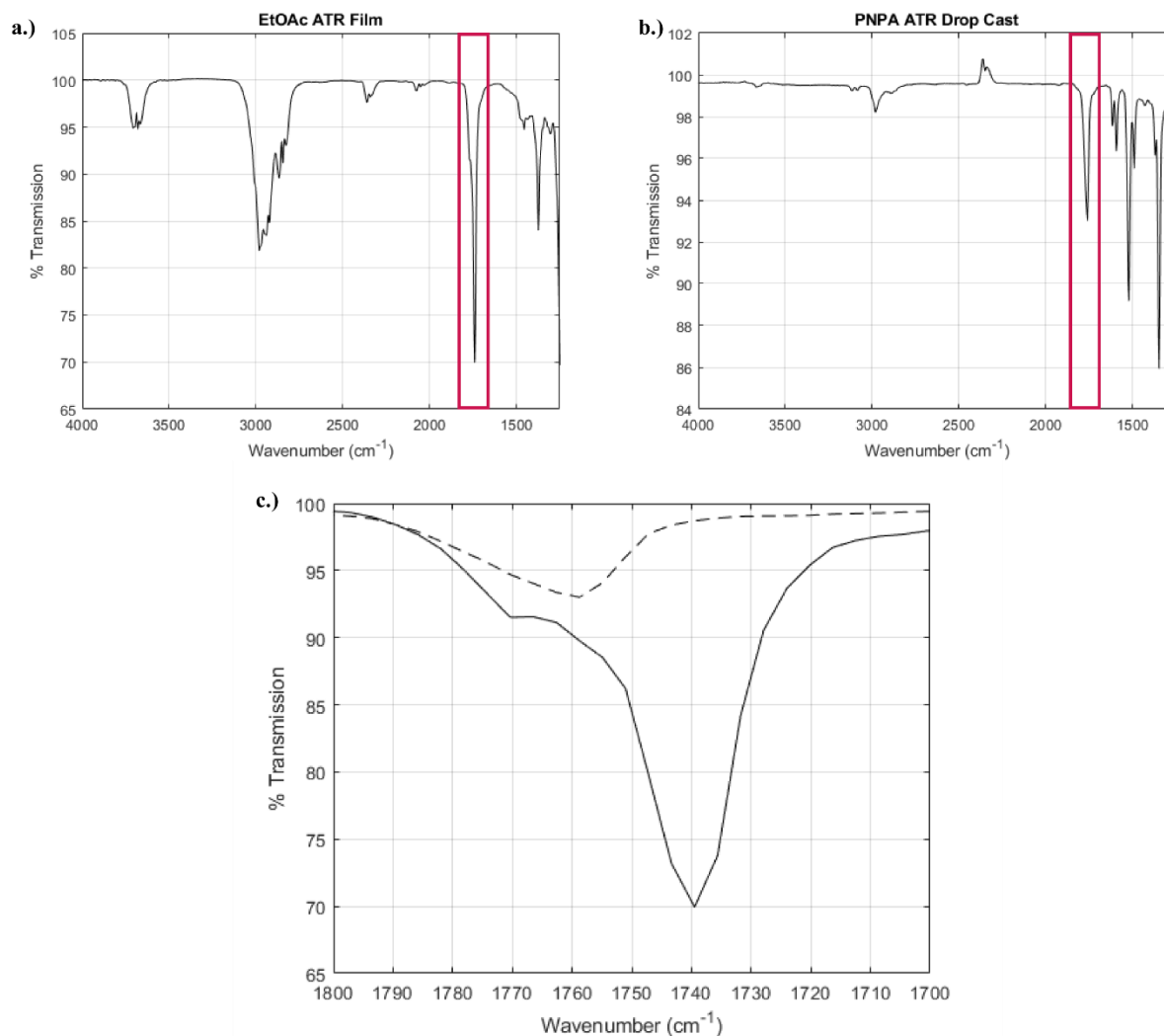


**Fig 14.** ATR-FTIR Spectra of coupled compounds used in the reactions. (a) Full ATR spectra of a thin film of pure ethyl acetate. Carbonyl vibrational mode observed at  $1740\text{ cm}^{-1}$  (c) Full ATR spectra of drop cast pure PNPA. Carbonyl vibrational mode observed at  $1758\text{ cm}^{-1}$ . (c) Zoomed in spectra of (a,b) spectra region enclosed by the red boxes. Slight shoulder may be from trace acetic acid contamination from oxidization during ATR measurements. EtOAc represented by solid line and PNPA represented by dashed line.

In order to explore the impact that the relative position of the vibrational modes of EtOAc and PNPA have on the polariton system, a three oscillator model was constructed. Much like the 2x2 model previously discussed, a Hamiltonian with diagonal elements of a cavity mode and EtOAc mode was generated with the previously determined coupling constant ( $72\text{ cm}^{-1}$ ). Here, an additional vibration mode for PNPA was included. The coupling constant for PNPA was determined by applying a coefficient to the EtOAc coupling constant. This coefficient was obtained by taking the relative transition dipole moment between PNPA and EtOAc which was in turn found by carbonyl peak integration of each compound. The estimated PNPA coupling constant (9.25) was found to yield UP and LP positions that reasonably reflect the observed experimental values.

As with the previous 2x2 model, the EtOAc and PNPA vibrational frequencies were set to the observed values ( $1742\text{ cm}^{-1}$  and  $1758\text{ cm}^{-1}$ ) and the Hamiltonian was solved for a range of cavity modes. The results yield a dispersion curve that closely resembles the UP and LP energies of the 2x2 model, however a third mode, the MP was found to match extremely closely to the molecular mode of the PNPA. For each coupled model produced from the three oscillator Hamiltonian, the Hopfield coefficients were plotted. The UP and LP modes showed to be significantly composed of the cavity and EtOAc, with equivalent contributions at the zero detuning condition. However, the UP and LP modes showed a minimal amount of contribution from PNPA. Conversely, the MP mode Hopfield coefficients showed the inverse. PNPA was the dominant character of the MP, with the cavity and EtOAc providing minimal contribution. This indicates that, while the EtOAc is strongly coupling with the cavity and delocalizing the vibrational modes across the UP and LP, the PNPA is remaining highly localized and behaving as a mostly uncoupled molecule. The results of the simulation are shown in table T1.

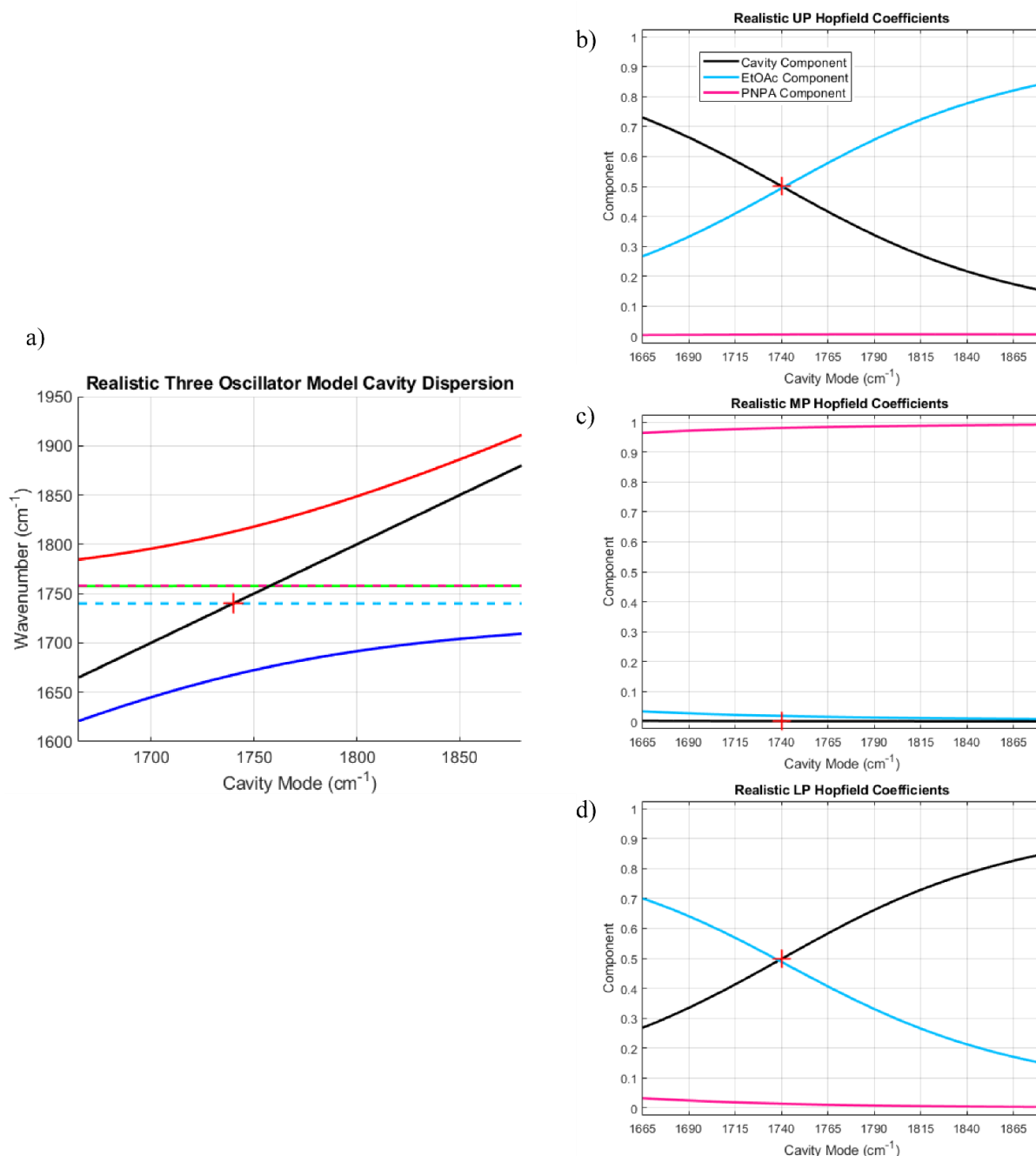


**Fig 15.** Results of 3x3 Hamiltonian model with frequencies determined from this work. EtOAc  $\omega_{\text{mol}} = 1740 \text{ cm}^{-1}$  and PNPA  $\omega_{\text{mol}} = 1758 \text{ cm}^{-1}$ . (a) Dispersion of 3x3 model. UP, MP, and LP are represented by red, green, and blue lines respectively. Dashed pink and green line represent overlapped frequencies of PNPA and MP. Cyan line indicates molecular frequency of EtOAc. Cavity mode represented by black line. Red cross indicates cavity mode and molecular mode resonant frequency. (b) Hopfield coefficients of cavity, EtOAc, and PNPA contributions to UP across cavity detuning. Cavity mode UP character (black line) and EtOAc UP character (cyan line) make up majority contribution. PNPA contribution to UP (pink line) is near zero across detuning. (c) Similar plot to (b) showing Hopfield coefficients contributions to MP. Note inversion of character, where MP is composed nearly entirely of PNPA. (d) Similar plot to (b) and (c) showing Hopfield coefficients contributions to LP.

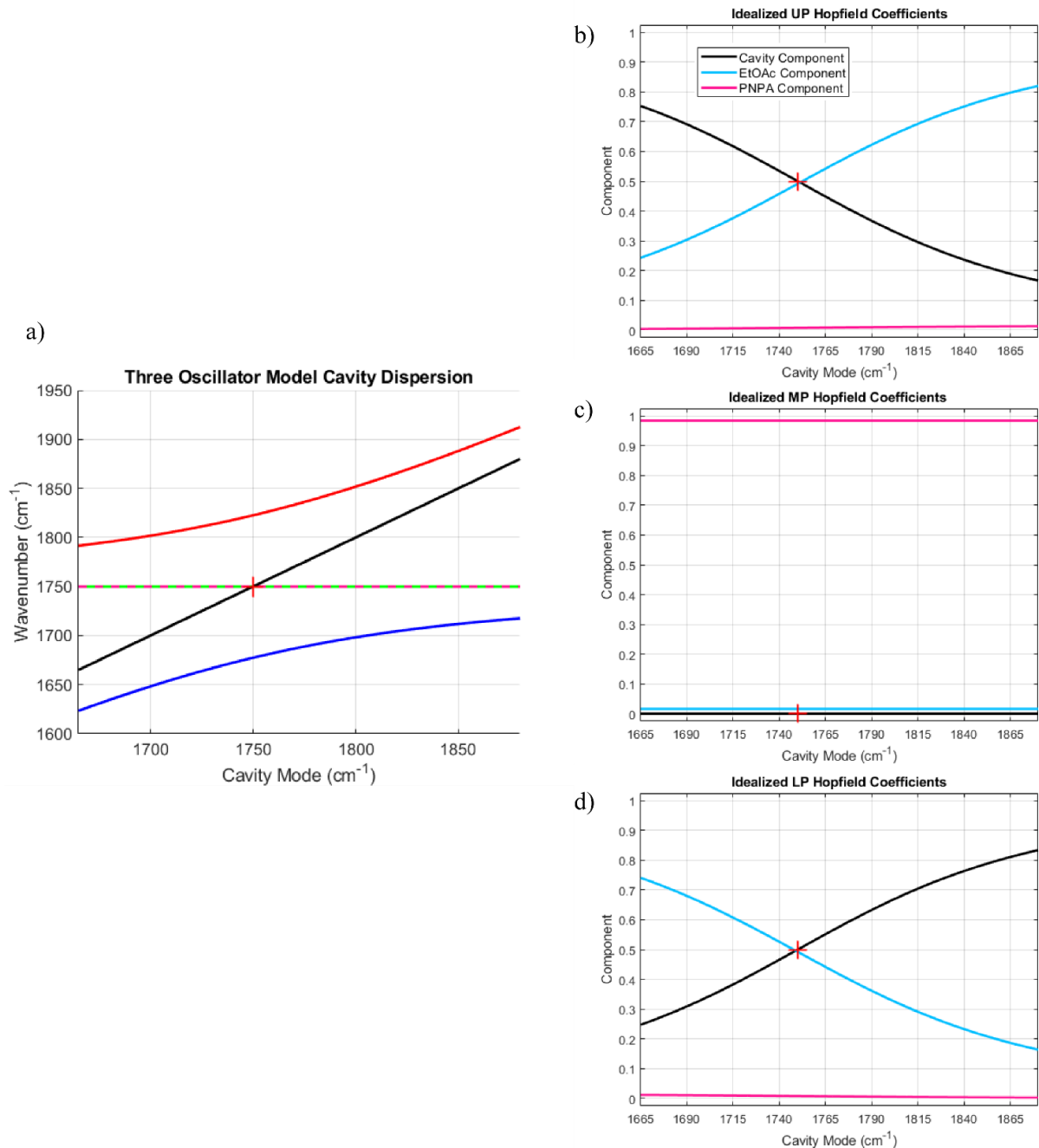


**Fig 16.** Results of 3x3 Hamiltonian model with idealized frequencies. EtOAc  $\omega_{\text{mol}} = 1750 \text{ cm}^{-1}$  and PNPA  $\omega_{\text{mol}} = 1750 \text{ cm}^{-1}$ . (a) Dispersion of 3x3 model. UP, MP, and LP are represented by red, green, and blue lines respectively. Dashed pink and green line represent perfectly overlapped molecular frequencies of PNPA and EtOAc. Cavity mode represented by black line. Red cross indicates cavity mode and molecular mode resonant frequency. (b) Hopfield coefficients of cavity, EtOAc, and PNPA contributions to UP across cavity detuning. Cavity mode UP character (black line) and EtOAc UP character (cyan line) make up majority contribution. PNPA contribution to UP (pink line) is near zero across detuning. (c) Similar plot to (b) showing Hopfield coefficients contributions to MP. Note inversion of character, where MP is composed nearly entirely of PNPA. (d) Similar plot to (b) and (c) showing Hopfield coefficients contributions to LP.



In order to fully examine the role of molecular vibrational mode positions in the VSC system, an “idealized” model was constructed. Here, the PNPA and EtOAc vibrational modes are both set to  $1750\text{ cm}^{-1}$  to maximize the ability for the molecules to cooperatively contribute to the polariton modes at the zero detuning condition. Despite this, the results remained relatively unchanged, with EtOAc and cavity modes showing strong delocalization over the UP and LP modes and PNPA remaining localized in the MP. The relevant values of the “idealized” model are shown in table T2.

**Table T1.** Tables showing Hopfield coefficients from the “realistic” three oscillator model when cavity is on resonance to EtOAc vibrational mode. UP, MP, and LP character corresponds to red cross indicated in Fig 13,14 (b-d).

Table T1	Realistic Frequencies	g	UP Character	MP Character	LP Character
Cav	$1740\text{ cm}^{-1}$	X	0.5006	0.0011	0.4982
PNPA	$1758\text{ cm}^{-1}$	9.25	0.0066	0.9832	0.0102
EtOAc	$1740\text{ cm}^{-1}$	72	0.4941	0.0183	0.4876

**Table T2.** Tables showing Hopfield coefficients from the “idealized” three oscillator model when cavity is on resonance to EtOAc vibrational mode. UP, MP, and LP character corresponds to red cross indicated in Fig 13,14 (b-d).

Table T2	Ideal Frequencies	g	UP Character	MP Character	LP Character
Cav	$1750\text{ cm}^{-1}$	X	0.5000	0.0000	0.5000
PNPA	$1750\text{ cm}^{-1}$	9.25	0.0081	0.9838	0.0081
EtOAc	$1750\text{ cm}^{-1}$	72	0.4919	0.0162	0.4919

The results of these simulations indicate that each molecular population will independently interact with the cavity. Of these coupling interactions, the strengths (coupling constant) are dictated strictly by the number of molecules in each population and that the cooperative effect is not present. In essence, the simulation indicates the ester hydrolysis of PNPA is not happening under VSC but more so that it is occurring in a solvent that is under VSC with minimal participation. This model is limited however, in that it treats each molecular

species as a single homogenous oscillator. As such, the model may be more accurately refined by treating each molecule as an oscillator with a coupling constant. However, this method is limited by computational power as each molecule in the model will require a term in the Hamiltonian. Due to the number of molecules present in the real system, only a fraction of these molecules can be included in such a simulation.

#### **4.6 Discrepancies of Results**

Despite all efforts taken to accurately reproduce the experimental conditions, the findings were not reproducible. Previously discussed, the crucial factor of the vibrational energy of EtOAc remains uncertain. Additionally, other factors that may have led to the discrepancies of results. The reaction volume in this work was reduced from the original work, from 300  $\mu\text{L}$  to 100  $\mu\text{L}$ . This was done to reduce the amount of “dead volume” in the cell, volume in the channels and tubing that are not within the cavity, but still undergoing reaction. Upon rough calculation, corroborated by Ref<sup>19</sup> the volume of the cavity was found to be 3  $\mu\text{L}$ . Should the reaction be accelerated under VSC, diffusion of uncoupled reactant solution would affect the reaction rate observed. Additionally, several reaction trials needed to be discarded due to sealing issues in the cell. Loss of solvent may artificially increase concentration of reactants as the reaction proceeds. Another possibility is from the method of data processing and UV-Vis spectra of the reactions. As previously discussed, the cavity maintained a moderately high Q-factor in the 400 nm regime. This resulted in a fringe pattern that complicated the tracing of the growth of the reaction product absorbance. In order to overcome this, the kinetic traces were obtained by integrating a range of 10 nm about the peak of the absorbance feature. When using a single wavelength, small shifts in the fringe pattern introduced a much larger variation and error in reaction traces. The low overall UV-Vis absorbance also narrowed the margin of error in simple

mounting of the cell within the instrument and cleanliness of the window surfaces. Great care was required in the securing of the cell such that it does not shift to a different angle within the spectrometer, artificially introducing a longer pathlength through the cell. Any residue on the surface of the cavity mirrors also introduced error and shifts in the baseline of the spectra.

## Chapter 5: Conclusion

The work presented shows efforts to reproduce to observations of Lather *et.al.*<sup>19</sup> which demonstrated the modification a chemical reaction rate by cooperative vibrational strong coupling. The conditions were rigorously studied in order to accurately replicate all aspects of the original experimental methods. Despite this, the results of the experiment showed an inability to replicate the findings. No significant change in reaction rate and no clear detuning dependence was observed. Investigation was further conducted using two and three oscillator models as well as transfer matrix method models to determine the validity of the results and help to explain the discrepancy in findings. These findings differ from other simulated results where VSC on the single molecule regime indicate reaction modification<sup>11,21,27,28</sup> but agree with those that simulate the collective molecule regime.<sup>12,22,23,29</sup> While all variables were controlled to the greatest extent possible, some differences were noted. Additionally, the limited fundamental understanding of the mechanism by which reaction modification by VSC may occur indicates that there may be other variables unknown to the scientific community that are vital to its function.

The results of this work are not only to demonstrate an inability to reproduce the findings of a previously observed VSC modified reaction, but to underline the necessity for further investigation of these systems. Developments in the reproducibility of VSC modified reactions have previously been underway and also struggled to achieve the prescribed results.<sup>30</sup> Due to the

immense impact VSC chemistry may have on chemical synthesis, it is paramount to have a thorough understanding of the key factors and components needed to rationally design future implementations. As with any emerging field or frontier phenomena with such potential, polariton chemistry remains a hotbed for debate and investigation.<sup>31,32</sup> It is hoped that this work provides some insights to guide future developments in understanding the fundamental mechanisms at play and further the field towards practical application of this promising new phenomena.

The material presented is a reprint of the publication by Wiesehan, G. D.; Xiong, W. Negligible Rate Enhancement from Reported Cooperative Vibrational Strong Coupling Catalysis. *J. Chem. Phys.* **2021**, *155* (24), 241103. <https://doi.org/10.1063/5.0077549>. The thesis author was the primary investigator and author of this material.

## References

- (1) Simpkins, B. S.; Dunkelberger, A. D.; Owrutsky, J. C. Mode-Specific Chemistry through Vibrational Strong Coupling (or *A Wish Come True* ). *J. Phys. Chem. C* **2021**, *125* (35), 19081–19087. <https://doi.org/10.1021/acs.jpcc.1c05362>.
- (2) Ebbesen, T. W. Hybrid Light–Matter States in a Molecular and Material Science Perspective. *Acc. Chem. Res.* **2016**, *49* (11), 2403–2412. <https://doi.org/10.1021/acs.accounts.6b00295>.
- (3) Hirai, K.; Hutchison, J. A.; Uji-i, H. Recent Progress in Vibropolaritonic Chemistry. *ChemPlusChem* **2020**, *85* (9), 1981–1988. <https://doi.org/10.1002/cplu.202000411>.
- (4) Kéna-Cohen, S.; Yuen-Zhou, J. Polariton Chemistry: Action in the Dark. *ACS Cent. Sci.* **2019**, *5* (3), 386–388. <https://doi.org/10.1021/acscentsci.9b00219>.
- (5) Long, J. P.; Simpkins, B. S. Coherent Coupling between a Molecular Vibration and Fabry–Perot Optical Cavity to Give Hybridized States in the Strong Coupling Limit. *ACS Photonics* **2015**, *2* (1), 130–136. <https://doi.org/10.1021/ph5003347>.
- (6) Nagarajan, K.; Thomas, A.; Ebbesen, T. W. Chemistry under Vibrational Strong Coupling. *J. Am. Chem. Soc.* **2021**, *143* (41), 16877–16889. <https://doi.org/10.1021/jacs.1c07420>.
- (7) Shalabney, A.; George, J.; Hutchison, J.; Pupillo, G.; Genet, C.; Ebbesen, T. W. Coherent Coupling of Molecular Resonators with a Microcavity Mode. *Nat. Commun.* **2015**, *6* (1), 5981. <https://doi.org/10.1038/ncomms6981>.
- (8) Wang, D. S.; Yelin, S. F. A Roadmap Toward the Theory of Vibrational Polariton Chemistry. *ACS Photonics* **2021**, *8* (10), 2818–2826. <https://doi.org/10.1021/acsp Photonics.1c01028>.
- (9) Xiang, B.; Xiong, W. Molecular Vibrational Polariton: Its Dynamics and Potentials in Novel Chemistry and Quantum Technology. *J. Chem. Phys.* **2021**, *155* (5), 050901. <https://doi.org/10.1063/5.0054896>.
- (10) George, J.; Shalabney, A.; Hutchison, J. A.; Genet, C.; Ebbesen, T. W. Liquid-Phase Vibrational Strong Coupling. *J. Phys. Chem. Lett.* **2015**, *6* (6), 1027–1031. <https://doi.org/10.1021/acs.jpcllett.5b00204>.

- (11) Du, M.; Campos-Gonzalez-Angulo, J. A.; Yuen-Zhou, J. Nonequilibrium Effects of Cavity Leakage and Vibrational Dissipation in Thermally Activated Polariton Chemistry. *J. Chem. Phys.* **2021**, *154* (8), 084108. <https://doi.org/10.1063/5.0037905>.
- (12) Schäfer, C.; Flick, J.; Ronca, E.; Narang, P.; Rubio, A. Shining Light on the Microscopic Resonant Mechanism Responsible for Cavity-Mediated Chemical Reactivity. *ArXiv210412429 Phys. Physicsquant-Ph* **2021**.
- (13) Galego, J.; Garcia-Vidal, F. J.; Feist, J. Cavity-Induced Modifications of Molecular Structure in the Strong-Coupling Regime. *Phys. Rev. X* **2015**, *5* (4), 041022. <https://doi.org/10.1103/PhysRevX.5.041022>.
- (14) Du, M.; Yuen-Zhou, J. Can Dark States Explain Vibropolaritonic Chemistry? *ArXiv210407214 Quant-Ph* **2021**.
- (15) Climent, C.; Feist, J. On the SN2 Reactions Modified in Vibrational Strong Coupling Experiments: Reaction Mechanisms and Vibrational Mode Assignments. *Phys. Chem. Chem. Phys.* **2020**, *22* (41), 23545–23552. <https://doi.org/10.1039/D0CP04154H>.
- (16) Vergauwe, R. M. A.; Thomas, A.; Nagarajan, K.; Shalabney, A.; George, J.; Chervy, T.; Seidel, M.; Devaux, E.; Torbeev, V.; Ebbesen, T. W. Modification of Enzyme Activity by Vibrational Strong Coupling of Water. *Angew. Chem. Int. Ed.* **2019**, *58* (43), 15324–15328. <https://doi.org/10.1002/anie.201908876>.
- (17) Hiura, H.; Shalabney, A.; George, J. Vacuum-Field Catalysis: Accelerated Reactions by Vibrational Ultra Strong Coupling. *13*.
- (18) Thomas, A.; Lethuillier-Karl, L.; Nagarajan, K.; Vergauwe, R. M. A.; George, J.; Chervy, T.; Shalabney, A.; Devaux, E.; Genet, C.; Moran, J.; Ebbesen, T. W. Tilting a Ground-State Reactivity Landscape by Vibrational Strong Coupling. *Science* **2019**, *363* (6427), 615–619. <https://doi.org/10.1126/science.aau7742>.
- (19) Lather, J.; Bhatt, P.; Thomas, A.; Ebbesen, T. W.; George, J. Cavity Catalysis by Cooperative Vibrational Strong Coupling of Reactant and Solvent Molecules. *Angew. Chem. Int. Ed.* **2019**, *58* (31), 10635–10638. <https://doi.org/10.1002/anie.201905407>.

- (20) Wiesehan, G. D.; Xiong, W. Negligible Rate Enhancement from Reported Cooperative Vibrational Strong Coupling Catalysis. *J. Chem. Phys.* **2021**, *155* (24), 241103. <https://doi.org/10.1063/5.0077549>.
- (21) Tichauer, R. H.; Feist, J.; Groenhof, G. Multi-Scale Dynamics Simulations of Molecular Polaritons: The Effect of Multiple Cavity Modes on Polariton Relaxation. *J. Chem. Phys.* **2021**, *154* (10), 104112. <https://doi.org/10.1063/5.0037868>.
- (22) Haugland, T. S.; Ronca, E.; Kjørstad, E. F.; Rubio, A.; Koch, H. Coupled Cluster Theory for Molecular Polaritons: Changing Ground and Excited States. *Phys. Rev. X* **2020**, *10* (4), 041043. <https://doi.org/10.1103/PhysRevX.10.041043>.
- (23) Li, X.; Mandal, A.; Huo, P. Cavity Frequency-Dependent Theory for Vibrational Polariton Chemistry. *Nat. Commun.* **2021**, *12* (1), 1315. <https://doi.org/10.1038/s41467-021-21610-9>.
- (24) Hutchison, J. A.; Schwartz, T.; Genet, C.; Devaux, E.; Ebbesen, T. W. Modifying Chemical Landscapes by Coupling to Vacuum Fields. *Angew. Chem. Int. Ed.* **2012**, *51* (7), 1592–1596. <https://doi.org/10.1002/anie.201107033>.
- (25) Connors, K. Chemical Kinetics: The Study of Reaction Rates in Solution, Chapter 2: Simple Rate Equations. In *Chemical Kinetics: The Study of Reaction Rates in Solution*; VCH: New York, N.Y., 1990.
- (26) Kolling, O. W. FTIR Study of the Solvent Influence on the Carbonyl Absorption Peak of Ethyl Acetate. *J. Phys. Chem.* **1992**, *96* (15), 6217–6220. <https://doi.org/10.1021/j100194a025>.
- (27) Vurgaftman, I.; Simpkins, B. S.; Dunkelberger, A. D.; Owrutsky, J. C. Negligible Effect of Vibrational Polaritons on Chemical Reaction Rates via the Density of States Pathway. *J. Phys. Chem. Lett.* **2020**, *11* (9), 3557–3562. <https://doi.org/10.1021/acs.jpcllett.0c00841>.
- (28) Li, T. E.; Nitzan, A.; Subotnik, J. E. On the Origin of Ground-State Vacuum-Field Catalysis: Equilibrium Consideration. *J. Chem. Phys.* **2020**, *152* (23), 234107. <https://doi.org/10.1063/5.0006472>.
- (29) Sidler, D.; Schäfer, C.; Ruggenthaler, M.; Rubio, A. Polaritonic Chemistry: Collective Strong Coupling Implies Strong Local Modification of Chemical Properties. *J. Phys. Chem. Lett.* **2021**, *12* (1), 508–516. <https://doi.org/10.1021/acs.jpcllett.0c03436>.

- (30) Imperatore, M. V.; Asbury, J. B.; Giebink, N. C. Reproducibility of Cavity-Enhanced Chemical Reaction Rates in the Vibrational Strong Coupling Regime. *J. Chem. Phys.* **2021**, *154* (19), 191103. <https://doi.org/10.1063/5.0046307>.
- (31) Shin, H.-H.; Koo, J.-J.; Lee, K. S.; Kim, Z. H. Chemical Reactions Driven by Plasmon-Induced Hot Carriers. *Appl. Mater. Today* **2019**, *16*, 112–119. <https://doi.org/10.1016/j.apmt.2019.04.018>.
- (32) Baffou, G.; Quidant, R. Nanoplasmonics for Chemistry. *Chem. Soc. Rev.* **2014**, *43* (11), 3898. <https://doi.org/10.1039/c3cs60364d>.